The Genesis of Severe, Long-Lived Bow Echoes

MORRIS L. WEISMAN

National Center for Atmospheric Research, Boulder, Colorado*

(Manuscript received 31 August 1991, in final form 26 May 1992)

ABSTRACT

A series of idealized simulations using a nonhydrostatic cloud model is used to investigate the genesis of bow echoes (a bow-shaped system of convective cells that is especially noted for producing long swaths of damaging surface winds). It is hypothesized that severe, long-lived bow echoes represent a dynamically unique form of mesoconvective organization being produced for a restricted range of environmental conditions, including a convective available potential energy (CAPE) of at least 2000 $m^2 s^{-2}$ and vertical wind shears of at least 20 $m s^{-1}$ over the lowest 2.5–5 km AGL. The key structural features include a 40–100-km-long bow-shaped segment of convective cells, with a strong rear-inflow jet extending to the leading edge of the bow at 2–3 km AGL, and cyclonic and anticyclonic eddies (referred to as "bookend" vortices) on the northern and southern flanks of the bowed segment, respectively. This structure characteristically develops three to four hours into the lifetime of a convective system and may remain coherent for several hours.

The evolution of this coherent structure occurs systematically as the convectively produced cold pool strengthens over time, eventually producing a circulation that overwhelms the ambient shear. This forces the convective cells to advect rearward above the cold air and weaken. The horizontal buoyancy gradients along the back edge of these rearward-advecting cells subsequently generate an elevated rear-inflow jet that extends to near the leading edge of the cold pool. The circulation of this jet helps negate the circulation of the cold pool, reestablishing deep, forced lifting at the leading edge of the system. This elevated rear-inflow jet is also enhanced through the development of bookend vortices. Such vortices are produced at the ends of a convective line segment as vortex lines inherent in the ambient vertically sheared environment are first tilted upward by the convective updrafts and then tilted downward and stretched by the convective downdrafts. The development of these features requires both large amounts of CAPE and strong vertical wind shear in the environment of these systems, as is consistent with the observed environments of many severe, long-lived bow echoes.

1. Introduction

The identification and understanding of convective structures that are coherent in both space and time have been ongoing goals of convective research. These structures are intriguing not only due to their unique dynamical character but also due to their enhanced predictability. Many of these structures have been the subject of previous inquiry, the supercell being a notable example (e.g., Klemp 1987). In this paper, we will discuss a long-lived mesoconvective structure that takes the form of a 60–100-km long bow-shaped segment of cells and that evolves either from an isolated cell or as part of a larger-scale squall line. These "bow echoes" (Fujita 1978) have been identified on radar for more than 30 years and are especially noted for producing long swaths of damaging surface winds. However, the physical mechanisms responsible for their structure and longevity have yet to be explained. In the following, we will investigate bow echoes through a series of idealized simulations using a nonhydrostatic numerical cloud model. We will hypothesize, in particular, that certain severe, long-lived bow echoes represent a dynamically unique form of mesoconvective organization that occurs for a limited set of environmental conditions: in particular, large amounts of thermodynamic instability and strong low-level vertical wind shear.

The tendency for convective cells to organize into or be organized by mesoscale systems has been known for quite some time. Perhaps the most intensely investigated example is the squall line, which is observed to exist on scales ranging from 100 to over 1000 km (e.g., Houze and Hobbs 1982; Bluestein and Jain 1985). More recently, investigators have focused on a broader range of long-lived mesoscale convective systems (MCSs) (e.g., Maddox 1980; Houze et al. 1990), many of which begin as squall lines. In all of these cases, the system is envisioned to be composed of a sequence of shorter-lived, independent convective cells that contribute collectively to the much larger system-scale structure.

The first reference to a system-scale organization that is larger than cell scale but smaller than squall-line or

* The National Center for Atmospheric Research is sponsored by the National Science Foundation.

Corresponding author address: Dr. Morris L. Weisman, National Center for Atmospheric Research, P.O. Box 3000, Boulder, CO 80307-3000.

MCS scale was presented by Nolen (1959), who identified a structure referred to as a line echo wave pattern (LEWP), which he defined to be ". . . a configuration of radar echoes in which a line of echoes has been subjected to an acceleration along one portion and/or a deceleration along that portion of the line immediately adjacent, with a resulting sinusoidal mesoscale wave pattern in the line." Hamilton (1970) further elucidated the significance of LEWPs by noting the association of this feature with damaging straight-line winds and tornadoes. He also deduced that the echo bulge was associated with an intense mesohigh, with the crest of the feature associated with a mesolow. Strong, damaging winds were attributed to the intense pressure gradient produced by these mesoscale pressure features. The term "bow echo" was first coined by Fujita (1978) in reference to the "bulging" echoes of Hamilton (1970): these echoes could occur individually or as part of an LEWP as identified by Nolen (1959). Both Fujita and, more recently, Przybylinski and Gery (1983) emphasize the association of bow echoes with long swaths of damaging straight-line winds.

A typical morphology of radar echoes associated with a bow echo, as envisioned by Fujita (1978; referred to as a "downburst" in this reference), is presented in Fig. 1. The system usually begins as a single, large, and strong convective cell that may be relatively isolated or may be part of a more extensive squall line. As the strong surface winds develop, the initial cell evolves into a bow-shaped segment of cells, with the strongest winds occurring at the apex of the bow. The cells at the ends of the segment may appear to move rearward relative to the center of the bow. During the most intense phase of its life, the center of the bow may form a "spearhead," with cyclonic and anticyclonic motion of the cells on the left and right flanks of the bow. A strong rear-inflow jet with its core at the apex of the bow is thought to be associated with the bulging and speeding up of the radar echoes. This concentrated jet is proposed by Fujita to be the source of the damaging winds. During the declining stage, the system often evolves into a comma-shaped echo with a cyclonically rotating head. Many of these hypothesized flow features have recently been confirmed via Doppler radar observations of bow echo–type systems (e.g., Burgess and Smull 1990; Schmidt and Cotton 1989). While bow-shaped convective systems are observed to occur over over a wide range of time and space scales, the more organized, severe bow echoes described above typically range in size from about 40 to 120 km and often have lifetimes of several hours.

Even though the observations reveal an organization to the bow echo that is larger-than-cell scale, a significant number of the documented cases also suggest that individual supercells may be incorporated within the larger-scale structure (e.g., Przybylinski and DeCaire 1985; Schmidt and Cotton 1989; Johns and Leftwich 1988; Smith 1990). However, the frequent observation of bow echoes without apparent supercells suggests that supercell processes are not crucial to their existence.

A recent study by Johns and Hirt (1987) offers some additional insights into bow echoes through a climatological study of a related phenomenon, referred to as a "derecho." The term "derecho" is used to describe convective systems that produce straight-line convective wind gusts greater than 26 m s^{-1} within a concentrated area with a major axis length of at least 400 km. The gusts must also show a systematic pattern of progression, with no more than 3 h elapsing between successive wind damage events. Such systems have been observed to have lifetimes of as long as 18 h, producing a swath of damaging winds hundreds of kilometers wide and 1000 km long. During the period of May–August for the years 1980–83, Johns and Hirt identified 70 derecho cases in the United States, most of which occurred in the upper regions of the Midwest.

In identifying derechos, investigators generally attempt to distinguish between those convective systems that produce continuous swaths of damaging winds and those that are associated with more isolated, short-lived wind events. Beyond this, there is no identification of the type of convective structure producing the wind event. The damage swath produced by an isolated supercell or a line of supercells (not including tornadic

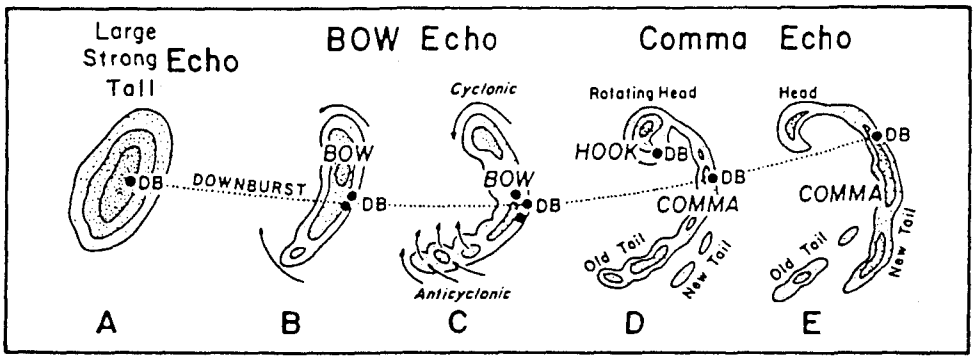

FIG. 1. A typical morphology of radar echoes associated with bow echoes that produce strong and extensive downbursts, labeled DB on the figure (from Fujita 1978).

events) may easily satisfy the criteria for a derecho event. However, an examination of the radar-echo configurations associated with these systems strongly suggests that the majority of cases involve bow echoes or LEWPs (Przybylinski and Decaire 1985; Johns and Hirt 1987).

Johns and Hirt found that the most significant attributes of the derecho environment were the extreme amounts of convective instability and low-level moisture. Surface dewpoints were commonly greater than 20°C, and the average lifted index was −9°C. In addition, wind strengths in the low-to-midtroposphere were greater than that for other types of severe-weather outbreaks. The average 500-mb winds were estimated to be 21 m s^{-1}, with the average 700-mb winds at 17 m s^{-1}. Also, over 80% of the events began along or to the north of an east–west oriented quasi-stationary thermal boundary and then moved along the boundary. The significance of this association is as yet unclear, but certain possibilities include the enhanced low-level convergence along the zone for triggering convective events, the enhanced instability that might be realized owing to the deepening of the moist layer along the zone, and the enhanced low-level vertical wind shear that would also be generated along such zones (i.e., such generation can be explained with thermal wind-type arguments). These environmental conditions have been established further in a more recent climatological study by Johns et al. (1990), and are also consistent with the environments observed for the individual bow echo cases referenced before.

The tendency for a convective cell to evolve into a bow-shaped system of cells for certain environments is documented in several of the previous modeling studies (e.g., Weisman and Klemp 1986). Fundamentally, an updraft produces rain that falls and evaporates, thereby producing a pool of cold air that spreads along the ground. This spreading cold pool produces convergence and lifting along its leading edge that can then trigger new cells. However, rather than a cold pool producing a complete circle of new cells around the initial storm, cells are favored along a bow-shaped arc oriented perpendicular to the vertical wind-shear vector. The ability to trigger new cells along this arc increases dramatically as the amount of vertical wind shear increases, and also increases if the wind shear is confined to the lowest 2–3 km AGL.

An explanation for this behavior is offered by Rotunno et al. (1988, hereafter RKW), who found that the best conditions for triggering cells along a spreading cold pool occur when the horizontal vorticity generated by the buoyancy gradient at the edge of the cold pool is matched by the opposing horizontal vorticity inherent in the ambient low-level vertical wind shear. In this situation, a vertical jet of air is created at the leading edge of the cold air that produces deeper lifting than if the shear were not present. This mechanism may, on its own, explain the strength and longevity of many of the observed convective systems that have been labeled as bow echoes. However, more recent simulations suggest that a unique dynamical structure may evolve within some of these systems that is not explained by the previous studies.

An example of such a feature occurs in a squall-line simulation previously presented by Weisman et al. (1988, hereafter WKR). The environmental conditions for this case include a convective available potential energy (CAPE) of 2400 m^2 s^{-2} and a unidirectional vertical wind shear of 25 m s^{-1} over the lowest 2.5 km AGL, with the vertical wind-shear vector oriented perpendicular to the squall line. The winds remain constant above 2.5 km. As described by WKR, the storm-induced cold pool remains well matched to the ambient shear throughout the simulation, with strong, erect cells continually being regenerated along the leading edge of the cold air. By 220 min (Fig. 2a), a 50-km-long line segment of cells has developed in the southern portion of the domain, with cyclonic and anticyclonic eddies apparent on the northern and southern ends of this line segment, respectively. More isolated cells are still scattered along the remaining portions of the line. Over the next 40 min, a strong rear-inflow jet develops behind the center of this line segment, and by 260 min, the rear inflow has intensified to greater than 20 m s^{-1} over the ambient flow. This structure is depicted at 300 min (Fig. 2b) and continues in quasi-steady fashion for an additional hour. A smaller bowed segment has developed north of the original feature, but does not retain its structure for as long a period of time.

The feature described in the above simulation represents a form of mesoconvective organization that has yet to be identified or investigated in numerical studies. The similarity between this feature and the available observations of bow echoes during the early part of their evolution (e.g., up to the comma-echo stage in Fig. 1) is intriguing. Common features include its bow shape and size, long life, intense rear-inflow jet with vortices on either side, and strong flow at the surface. In addition, both develop either from an isolated cell or as part of a squall line, and both occur for similar environmental conditions, consisting of large amounts of thermodynamic instability and strong low-level vertical wind shear. Finally, both are generated several hours into the life cycle of the convective system. It is thus hypothesized that the model-produced feature may be representative of many of the observed long-lived convective structures that have been labeled as bow echoes.

The goal of this paper is to document the physical processes that develop and maintain these long-lived mesoconvective structures. This will be accomplished through the analysis of idealized simulations that reproduce the bow-echo structure using the simplest possible set of initial conditions. The discussion will concentrate particularly on one simulation that traces the evolution of an isolated cell in a horizontally ho-

mogeneous environment with unidirectional vertical wind shear, using the same thermodynamic and wind profiles specified in the squall-line example discussed before. This simulation reproduces all the major features of the squall-line bow echo described in Fig. 2, including the midlevel vortices at the ends of convective segment and the strong, elevated rear-inflow jet. The analysis of these features, however, is greatly simplified by tracing the evolution of a single cell rather than the evolution of a complete squall line. This simulation will be referred to as the "idealized" bow echo.

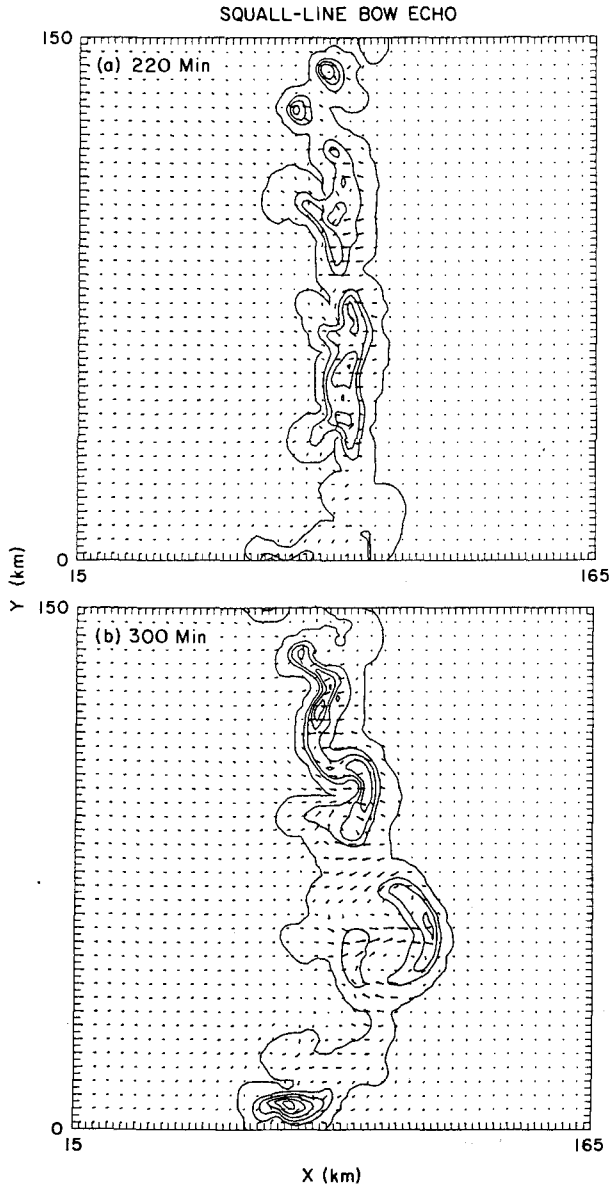

FIG. 2. Horizontal cross sections of system-relative flow and rainwater contours at 2.5 km AGL at (a) 220 min and (b) 300 min for the squall line simulation described by WKR, using an environmental vertical wind shear of 25 m s^{-1} over the lowest 2.5 km AGL. A domain speed of $U = 22.5$ m s^{-1} has been subtracted from the flow vectors. Vectors are plotted at every other grid point (a distance of two grid lengths represents 25 m s^{-1}). The rainwater field is contoured using a 2 g kg^{-1} interval. Only a 150 km × 150 km portion of the entire domain is shown.

The discussion begins in section 2 with a brief description of the numerical model used for this study, followed in section 3 by a detailed description of the evolution of the idealized bow echo. Section 4 presents an analysis of the rear-inflow jet based on the recent study of Weisman (1992), who considers the evolution of two-dimensional circulations via the horizontal vorticity equation. This analysis explains much of the rear-inflow characteristics along the center of the bow echo, but must be expanded in section 5 to consider the influence of the midlevel vortices that exist at the ends of the bowed system. In section 6, a set of simulations is presented that tests the sensitivity of the results to the details of the thermodynamic profile and the depth of the shear layer and helps clarify the environmental conditions most conducive to bow echo genesis. Finally, in section 7, the main findings of this study are summarized and discussed in the context of future research initiatives.

2. Model formulation and experimental design

The simulations to be described in this study were all completed using the three-dimensional nonhydrostatic numerical cloud model described by Klemp and Wilhelmson (1978), as also used by Weisman (1992). The model does not currently include ice processes or radiative heating. Open boundary conditions are employed on the lateral boundaries, and a gravity-wave radiation condition is employed at the upper boundary (Klemp and Durran 1983). Free-slip conditions are specified at the surface, with the vertical velocity set to zero.

Convective cells are initialized in a horizontally homogeneous environment that is characterized by specified vertical profiles of temperature, water vapor, and wind. In addition, the wind profiles are defined to be unidirectional, and the Coriolis force is set to zero. These conditions ensure a mirror-image symmetry to the solution about an axis directed parallel to the vertical wind-shear vector. Thus, only half of the full domain need be included. The effects of the Coriolis force and directionally varying vertical wind shears on system structure will be presented in a future study. Storms are initialized by placing an ellipsoidal warm thermal of 10-km horizontal and 1400-m vertical radius on the center of the symmetry axis. The thermal is given a maximum magnitude of 2°C at the center, which decreases to zero at the edge, and is balanced hydrostatically with the pressure field. Flow begins as air accelerates horizontally into the region of lowered pressure beneath the thermal, with the resultant convergence creating upward motion that releases the convective instability.

The simulations to be described all use a horizontal grid resolution of 2 km and a vertical grid resolution of 750 m. The domain size is 80 km in the y, or crosswind, direction; 160 km in the x, or alongwind, direction; and 17.5 km in the z, or vertical, direction. The symmetry axis is located along $y = 0$, and thus, the effective domain size in the y direction is also 160 km. Each simulation is run for 240 min. Several experiments were run to test the sensitivity of the results to this model formulation. In one experiment, the horizontal resolution was increased to 1 km, keeping the domain size the same. In another case, the vertical resolution was increased to 350 m at low levels, stretching uniformly to about 1 km at the top of the domain. In a third experiment, the original grid resolution was retained, but the domain was increased in size to 160 km along the y axis (effectively 320 km, including the mirror image) by 640 km along the x axis to test the effects of the boundaries. However, the present results were not significantly affected by any of these changes.

The environmental conditions used for the idealized bow echo simulation are identical to those used in the squall-line simulation discussed in the Introduction. The thermodynamic profile is characterized by a CAPE of 2377 $m^2 s^{-2}$ with relatively moist conditions throughout the troposphere (Fig. 3). Air that ascends from near the surface experiences a small amount of negative buoyancy before reaching the level of free convection (LFC) at 1.7 km AGL (820 mb). This thermodynamic profile was also used in the sensitivity studies of Weisman and Klemp (1982, 1984, 1986) and of WKR and RKW. Also included in Fig. 3 are additional temperature profiles used for the environmental sensitivity experiments to be described in section 6. A unidirectional wind profile is specified along the y axis, with the wind increasing linearly from zero at the surface to a maximum of $U_s = 25$ m s^{-1} at 2.5 km AGL, with constant winds above. The sensitivity of the results to variations in this wind profile will also be discussed in section 6.

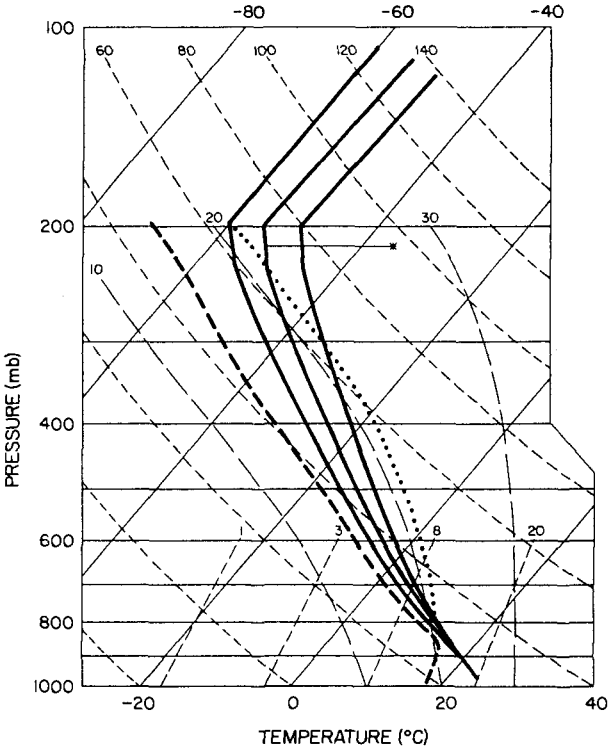

FIG. 3. Skew T-log$p$ diagram depicting the range of thermodynamic profiles used for the numerical simulations. The three temperature profiles are depicted by the thick solid lines, while the moisture profile is depicted by the thick dashed line. The temperature profile used for the idealized bow echo simulation is denoted by a star. The thick dotted line represents the parcel ascent curve for the 14 g kg^{-1} surface mixing ratio cases included in Table 1.

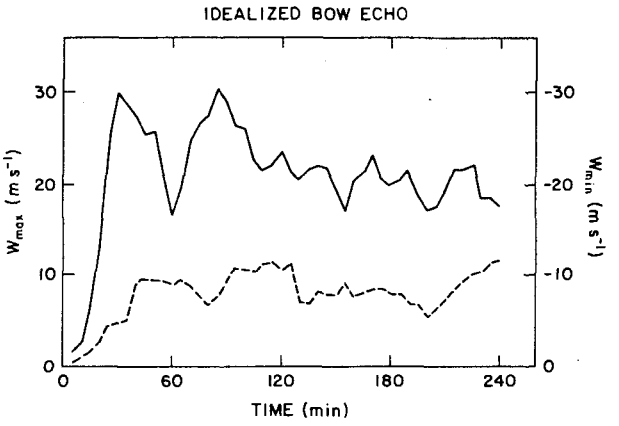

FIG. 4. Time series of maximum (solid) and minimum (dashed) vertical velocities (m s^{-1}) observed during the 240-min idealized bow echo simulation.

3. An idealized bow echo

a. General system characteristics

An overview of the evolution of the idealized bow echo is presented through a time series of the maximum and minimum vertical velocities (Fig. 4), along with horizontal cross sections depicting updraft and downdraft locations, rainwater concentration, and approximate system-relative flow at the surface and 2.5 km AGL at hourly intervals through 240 min (Figs. 5–8). The 2.5-km level was chosen as it clearly displays the evolution of the midlevel vortices and rear-inflow jet, which appear to be the distinguishing components of the bow-echo structure. Also, at this level, the system-relative ambient flow is close to zero, thereby accentuating the flow features generated by the convective system. The vertical structure of the system is summarized in Fig. 9 through vertical cross sections of rainwater concentration, equivalent potential temperature (θ_e), and system-relative flow along the symmetry axis of the simulation domain, also at hourly intervals.

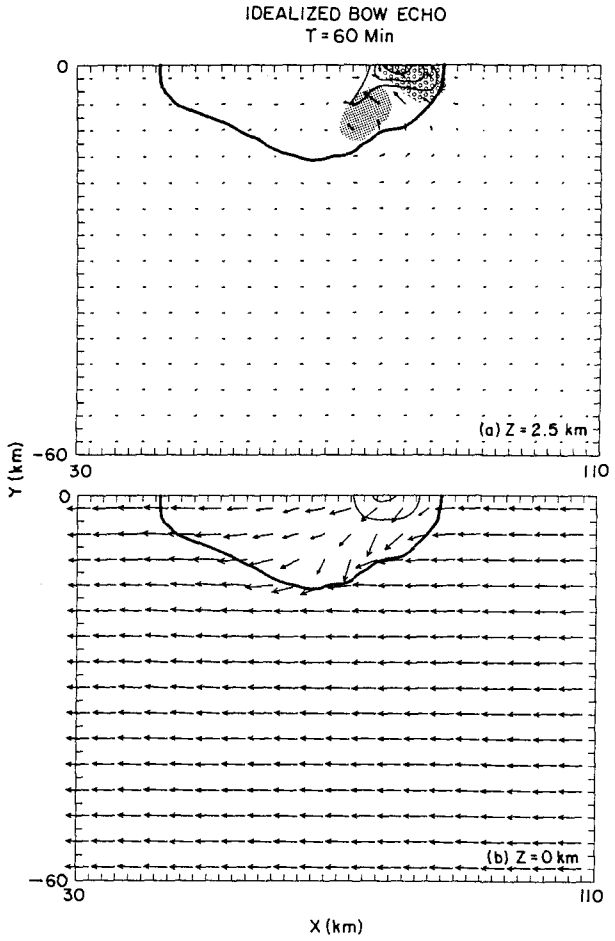

FIG. 5. Horizontal cross sections of rainwater concentration and flow vectors at (a) 2.5 km AGL and (b) 0 km AGL at 60 min for the idealized bow echo simulation. Vectors are presented at every other grid point, with a vector length of two grid intervals being equal to a magnitude of 25 m s^{-1}. A domain speed of U = 22.5 m s^{-1} is subtracted from the flow field. The ground-relative system propagation speed at this time is 18 m s^{-1}. The rainwater is contoured at 2 g kg^{-1} intervals, and the thick line represents the location of the gust front at the surface. For (a), regions of updraft greater than 4 m s^{-1} are shaded and regions of downdraft less than −2 m s^{-1} are stippled. The y = 0 boundary represents the axis of symmetry for the simulation, with only a 60 km × 80 km portion of the full domain presented.

The initial evolution follows that described in the previous modeling studies of Weisman and Klemp (1982, 1984, 1986) and WKR. The updraft triggered along the symmetry axis reaches a maximum strength of 30 m s^{-1} at about 30 min into the simulation (Fig. 4). This produces rainfall and evaporative cooling, resulting in the development of a downdraft and, subsequently, a cold pool that begins to spread along the surface. By 60 min, the surface flow has begun to diverge in response to the spreading cold air (Fig. 5b), with the downdraft intensifying to −9 m s^{-1} (Fig. 4). The original rain cell is still on the symmetry axis, near the leading edge of the gust front, but the updraft has split into a right- and left-moving pair in response to the strong vertical wind shear (Fig. 5a; note that only the right mover is shown). The vertical cross section at this time cuts through the original rain cell, displaying its essentially vertical orientation, with the remnants of the original updraft still evident near its top (Fig. 9a). As also described in RKW and WKR, the downdraft is fed from the front of the system, having originated at midlevels where θ_e is low, and spreads primarily rearward along the surface. The system propagation speed at this time (defined by the motion of the gust front relative to the ground) is 18 m s^{-1}.

The split updraft strengthens to 30 m s^{-1} by 85 min (Fig. 4), but weakens thereafter and becomes incorporated into a series of new cells that has developed along the gust front between the original splitting pair. By 120 min, the system has evolved into two 30-km-long bow-shaped system of cells, extending to both sides of the symmetry axis (Fig. 6), with updraft maxima reduced to 23 m s^{-1} and downdraft minima increased to −11 m s^{-1} (Fig. 4). The surface flow diverges 12 km behind the leading edge of these bow features, with

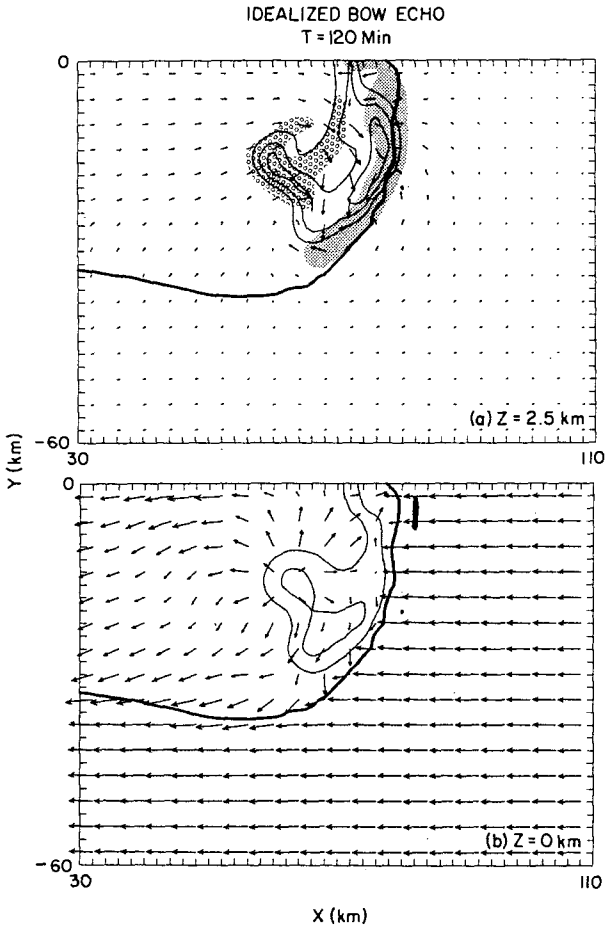

FIG. 6. Same as Fig. 5 but at 120 min. The ground-relative system propagation speed at this time is 22.5 m s^{-1}.

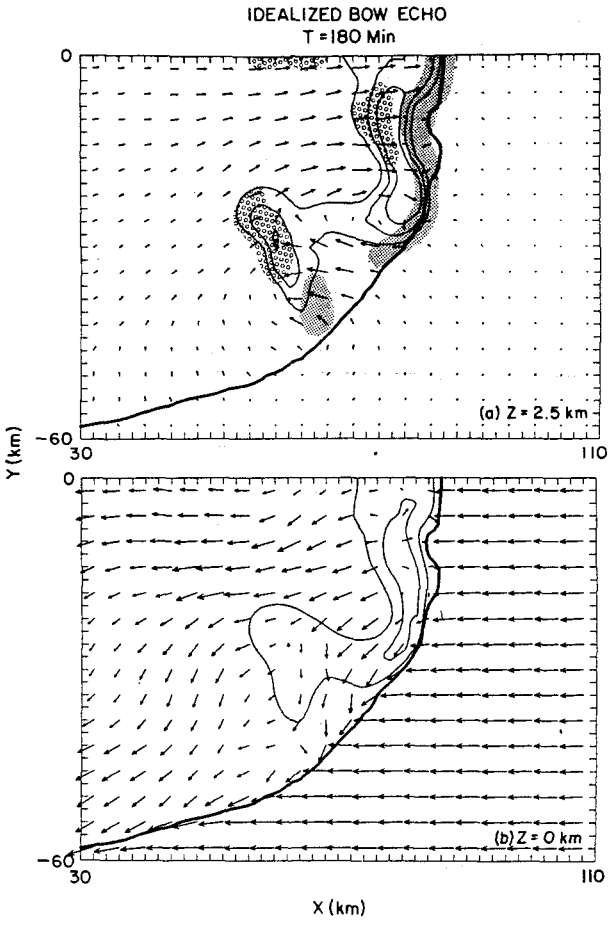

FIG. 7. Same as Fig. 5 but at 180 min. The ground-relative system propagation speed at this time is 27 m s^{-1}.

the ground-relative winds reaching speeds greater than 30 m s^{-1} (Fig. 6b). The remnants of the original split updraft at the southern end of the line segment are correlated with cyclonic vorticity at 2.5 km, but a large anticyclonic eddy is now also evident behind this updraft zone and is coincident with the downdraft and rain region. A mirror-image anticyclonic updraft and cyclonic downdraft exists at the northern end of the system, north of the symmetry axis (not shown). This vorticity is created as the vortex lines inherent in the ambient shear are tilted into the vertical by the updraft and then are tilted back down and stretched in the downdraft. This process is discussed in detail in section 5. The downdraft vortices at the ends of the convective line segment remain prominent throughout the simulation and are subsequently referred to as bookend vortices. A rear-inflow current has developed between the bookend vortices, with a strength of nearly 10 m s^{-1} close to each vortex (relative to the ambient 2.5-km flow; i.e., subtract 2.5 m s^{-1} from the vector magnitudes presented in the figures), but weakening to 3 m s^{-1} along the symmetry axis.

The vertical cross section along the symmetry axis at 120 min (Fig. 9b) passes through a newly developing cell, with a plume of high θ_e air from near the surface extending through the entire vertical extent of the storm. This updraft current still spreads predominantly downshear aloft. The downdraft at this location is not very strong, but low θ_e air from midlevels has begun to descend from the rear of the system. The system propagation speed at this time has increased to 22.5 m s^{-1}.

Between 120 and 180 min, the system continues to expand in size, with the rear inflow strengthening considerably along the symmetry axis (now 15 m s^{-1} relative to the ambient 2.5-km flow) and extending rearward nearly 40 km from the leading edge of the system (Fig. 7). It also expands in the vertical, reaching a depth of 3.5 km (Fig. 9c). The core of the jet remains at about 2.5 km AGL as it penetrates to near the leading edge of the gust front before being diverted upward and downward as it collides with the updraft current. Potentially cold midlevel air that supplies the downdraft and surface outflow circulation now feeds entirely

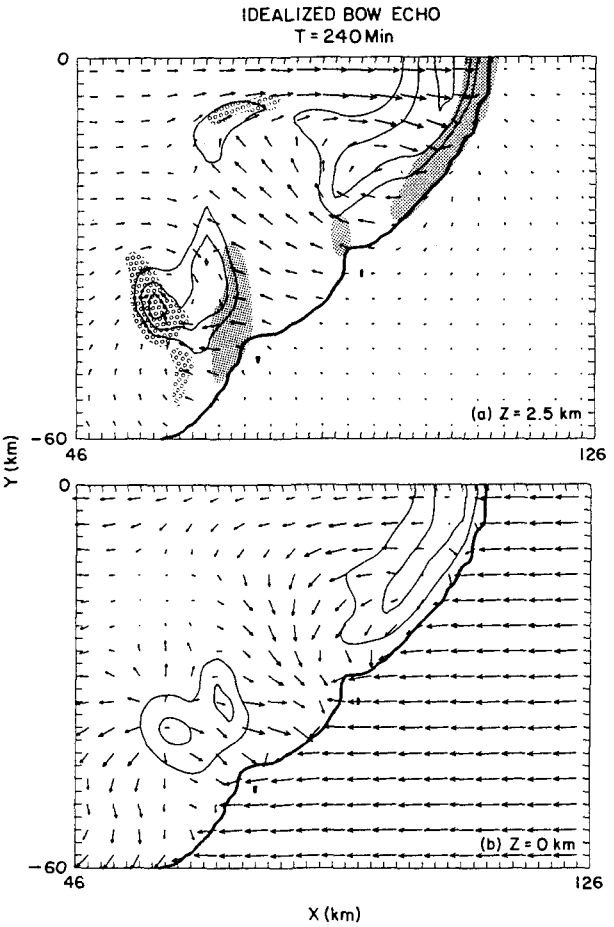

FIG. 8. Same as Fig. 5 but at 240 min. The ground-relative system propagation speed at this time is 29 m s^{-1}.

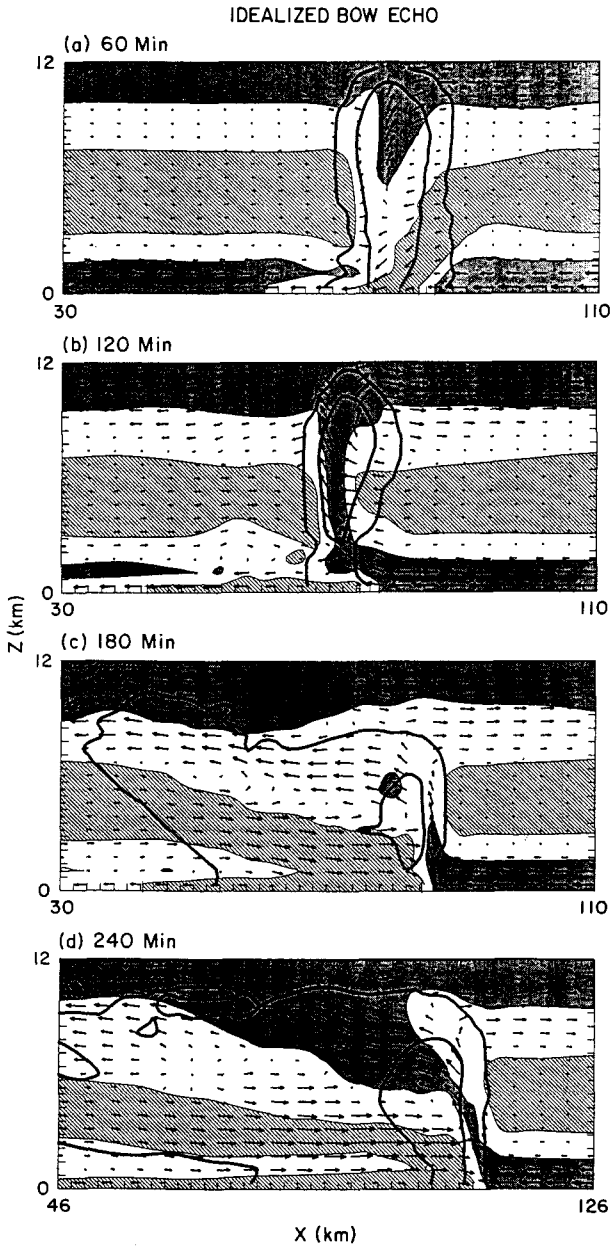

FIG. 9. Vertical cross sections of θ_e, flow vectors and rainwater concentration along the $y = 0$ boundary at (a) 60 min, (b) 120 min, (c) 180 min, and (d) 240 min for the idealized bow-echo simulation. Vectors are presented at every other grid point, with a vector length of two grid intervals being equal to a magnitude of 25 m s^{-1}. A domain speed of $U = 22.5$ m s^{-1} is subtracted from the flow field. The ground-relative system propagation speed is (a) 18 m s^{-1}, (b) 22.5 m s^{-1}, (c) 27 m s^{-1}, and (d) 29 m s^{-1}. Regions of θ_e greater than 334 K are darkly shaded, and regions less than 326 K are lightly shaded. Thick lines represent the 0 and 4 g kg^{-1} rainwater contours. Only an 80 km × 12 km portion of the domain is presented.

from the rear of the system, in association with the rear-inflow jet, with the cold pool increasing in depth to nearly 3 km at its leading edge. The updraft at the leading edge of the system is still vertically oriented through 5.5 km, but is much stronger in the lower levels than earlier. Above 5.5 km, however, most of the updraft current turns abruptly rearward (upshear), with a smaller proportion continuing on a vertical trajectory and exiting downshear at about 9 km. The surface flow now diverges just behind the leading edge of the gust front, with the strongest ground-relative winds confined to this narrow zone (Fig. 7b). The bookend vortices are still evident at the ends of the convective line segment, but have not changed in intensity during this period. The system propagation speed has further increased to 27 m s^{-1}, with updraft maxima remaining between 20 and 22 m s^{-1} and downdraft minima weakening to about −8 m s^{-1} (Fig. 4).

Figure 10 presents a series of air parcel trajectories that are representative of the flow during this phase of system development. Each trajectory is calculated using model data saved every 5 min, and originates at 180 min at the location indicated by a small dot. Air parcels that originate near the surface ahead of the system are lifted abruptly as they encounter the leading edge of the gust front. Parcels near the symmetry axis are lifted steeply through about 6 km and then proceed upward more gradually as they advect rapidly rearward relative to the leading edge of the system. Just away from this core region, parcels are not lifted as high initially but continue upward behind the system. The deepest ascent, however, occurs in the more isolated cells outside of the zone defined by the bookend vortices. Air parcels within the rear-inflow jet descend gradually from their origin at 3–4 km as they approach the leading edge of the system, with the lower portion of the jet then descending more abruptly and exiting rearward along the surface. The upper portion of the jet, however, diverts upward within the updraft and exits to the rear of the system at about 8–10 km. Since this rear-inflow air is potentially cold and convectively stable upon ascent, this suggests that this portion of the updraft must be strongly forced.

The rear inflow continues to strengthen and extend rearward over the next 30–60 min, reaching magni-

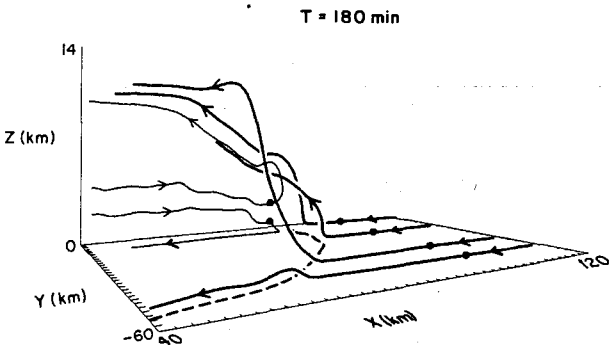

FIG. 10. Representative parcel trajectories for the idealized bow-echo simulation at 180 min. Dots represent the point of origin of each trajectory, with the trajectory integrated forward and backward in time from that point. The surface gust front at $t = 180$ min is denoted by the dashed line.

tudes greater than 20 m s^{-1} over much of the core region of the system, but the basic configuration that evolved by 180 min, consisting of the bookend vortices, elevated rear-inflow jet, and strong erect updraft through 6 km along the leading edge, remains essentially intact. The most significant change during this period is a narrowing of the distance between the bookend vortices between 180 and 240 min (Figs. 7a and 8a). This represents an intriguing aspect of the evolution of these features, but its explanation is beyond the scope of this study. In addition, the system propagation speed increases to 29 m s^{-1}. By 240 min, the rain field is in the form of a 50-km continuous bow extending between the bookend vortices, with more isolated, strong cells extending 25 km on either side of this primary feature (Fig. 8). The vertical cross section (Fig. 9d) depicts an even stronger and deeper rear-inflow current than earlier, with the lifting at the leading edge of the system also stronger and deeper. This basic structure is maintained for an additional 90 min (not shown), with the system propagation speed averaging about 27 m s^{-1}.

b. *Diagnostic pressure analysis*

An analysis of the pressure field at 180 min offers further insights into the forces creating and maintaining the intense circulation. For this purpose, the pressure is decomposed via a diagnostic pressure equation for anelastic Boussinesq flow, as described by Schlesinger (1980) and Rotunno and Klemp (1982, 1985):

$$\nabla\cdot(C_p\bar{\rho}\,\bar{\theta}_v\nabla\pi) = -\nabla\cdot(\bar{\rho}\,\mathbf{v}\cdot\nabla\mathbf{v}) + \frac{\partial B}{\partial z}; \quad (1)$$

where B represents the buoyancy, defined as

$$B \equiv g\left[\frac{\theta'}{\bar{\theta}} + 0.61(q_v - \bar{q}_v) - q_c - q_r\right]; \quad (2)$$

θ represents the potential temperature; q_v, q_c, and q_r represent the mixing ratio of water vapor, cloud water, and rainwater, respectively; and π represents the Exner function, defined as

$$\pi \equiv \left(\frac{p}{p_0}\right)^{R_d/C_p}. \quad (3)$$

Bars over individual variables refer to the initial undisturbed state, which is a function of z only, while primes refer to perturbations from this initial state. The first term on the rhs of (1) represents the contributions to the pressure field due to variations in the velocity field. The component of pressure derived from this term is often referred to as the dynamic pressure, π_{dn}. The expansion of this term (not shown) demonstrates how the dynamic pressure can be decomposed further into terms representing fluid extension and fluid shear. The fluid shear terms represent the rotational component of the flow and contribute to negative perturbations to the pressure field. The fluid extension terms are associated with converging and diverging flow and contribute to positive pressure perturbations.

The second term on the rhs of (1) represents contributions to the pressure field due to vertical variations in the buoyancy field. The component of pressure thus diagnosed is often referred to as the buoyancy pressure, π_b. These pressure perturbations are similar to those that would be derived by calculating the hydrostatic component of the pressure field, with negative pressure perturbations occurring beneath positive buoyancy perturbations, and vice versa. However, π_b represents a more accurate portrayal of the resultant pressure field since it considers the full three-dimensional effects of the buoyancy perturbations on the fluid.

A vertical cross section of the pressure perturbations and system-relative flow along the symmetry axis at 180 min is presented in Fig. 11. The pressure field is highlighted by a mesohigh near the surface, with a maximum magnitude of 3.5 mb behind the leading edge of the gust front, and a mesolow at midlevels, with a maximum magnitude of −1.5 mb at 3.5 km AGL, slightly to the rear of the surface mesohigh. The rear inflow accelerates in response to the negative horizontal pressure gradient associated with this mesolow, but decelerates and diverges vertically as it encounters a strong positive pressure gradient at the leading edge of the system. The decomposition of the pressure field reveals that the buoyancy pressure is the dominant contributor to both the mesolow and mesohigh. The dynamic terms contribute significantly only along the leading edge of the surface gust front, where the flow is strongly convergent.

A plan view of the pressure perturbations and system-relative flow at 180 min at 2.5 km AGL is presented in Fig. 12. The flow characteristics are similar to that portrayed in the vertical cross section, with the rear inflow accelerating into a midlevel mesolow and decelerating at the leading edge of the system. The pressure decomposition again suggests that the buoyancy terms are the dominant contributor to the pressure field. However, the dynamic terms off of the axis of symmetry are now seen to contribute significantly behind much of the leading edge of the gust front and especially in the region of the bookend vortex. This dynamic lowering of pressure is associated with the strong curvature of the flow field, which is due to the strong vertical circulation behind the gust front as well as the horizontal circulation associated with the bookend vortex. An additional vertical cross section taken closer to the bookend vortex (not shown) displays a pressure pattern similar to that depicted along the symmetry axis, with the exception that a 0.5–1-mb dynamic pressure low is evident behind the gust front, extending upward to 6 km AGL.

The forces accelerating the major flow components of the idealized bow echo can be traced more quantitatively through a Lagrangian analysis of the u com-

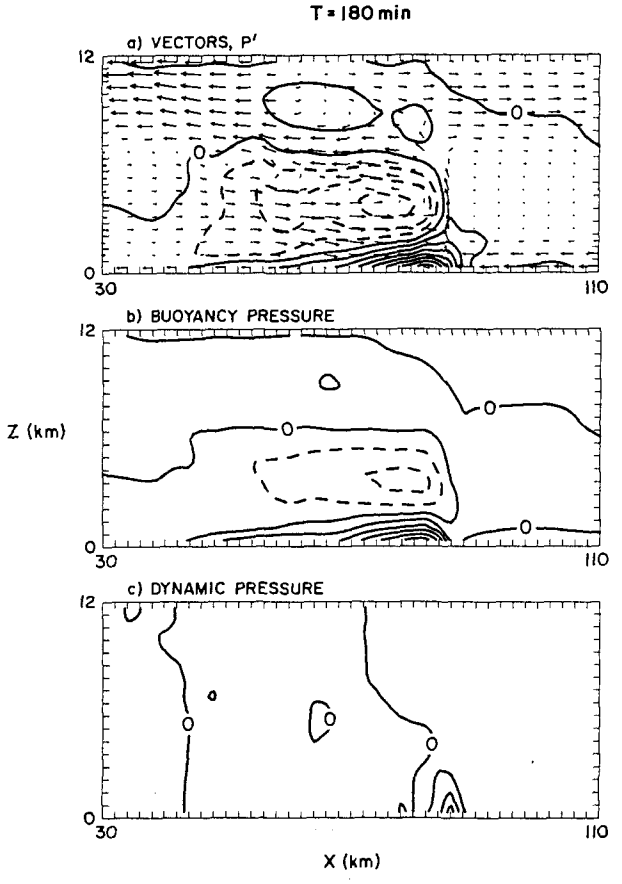

FIG. 11. Vertical cross section along the $y = 0$ axis of (a) pressure perturbations and flow vectors, (b) buoyancy contributions to the pressure field, and (c) dynamic contributions to the pressure field at 180 min for the idealized bow-echo simulation. The pressure field is contoured at 0.5-mb intervals, with the dashed and solid lines contouring negative and positive perturbations, respectively. The vectors are presented at every other grid point, with a vector length of two grid intervals being equal to a vector magnitude of 25 m s^{-1}. A domain speed of $U = 22.5$ m s^{-1} is subtracted from the flow field. The ground-relative system propagation speed at this time is 27 m s^{-1}.

ponent of the equation of motion, which may be written to display the contributions to u momentum from the dynamic and buoyancy pressure gradients separately (also ignoring mixing effects):

$$\frac{du}{dt} = -C_p\bar{\theta}_v\frac{\partial\pi_{dn}}{\partial x} - C_p\bar{\theta}_v\frac{\partial\pi_b}{\partial x}. \quad (4)$$

The individual contributions are determined by interpolating the terms along parcel trajectories feeding into the rear inflow and integrating the appropriate pressure gradients along the trajectories over time:

$$u_{dn} = \int_T - C_p\bar{\theta}_v\frac{\partial\pi_{dn}}{\partial x}\,dt, \quad (5)$$

$$u_b = \int_T - C_p\bar{\theta}_v\frac{\partial\pi_b}{\partial x}\,dt, \quad (6)$$

$$u = u_0 + u_{dn} + u_b, \quad (7)$$

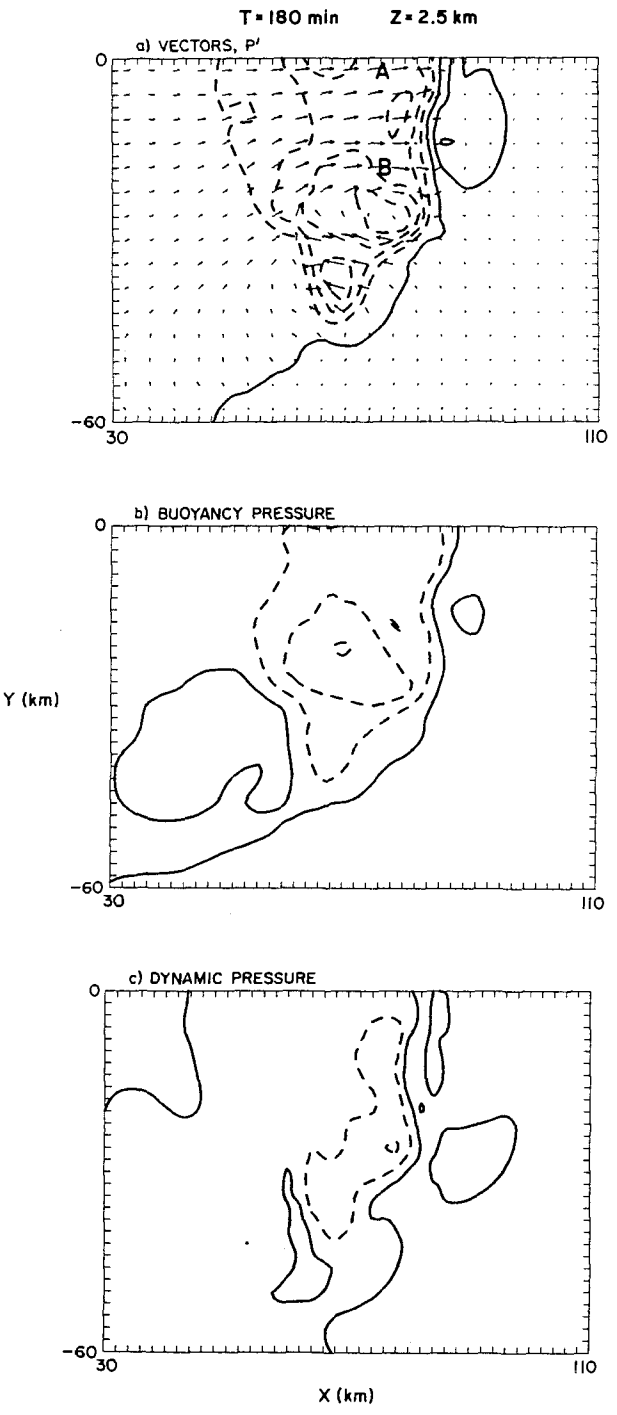

FIG. 12. Horizontal cross section at 2.5 km AGL of (a) pressure perturbations and flow vectors, (b) buoyancy contributions to the pressure field, and (c) dynamic contributions to the pressure field at 180 min for the idealized bow echo simulation. The pressure field is contoured at 0.5-mb intervals, with the dashed and solid lines contouring negative and positive perturbations, respectively. The vectors are presented at every other grid point, with a vector length of two grid intervals equal to a vector magnitude of 25 m s^{-1}. A domain speed of $u = 22.5$ m s^{-1} is subtracted from the flow field. The ground-relative system propagation speed at this time is 27 m s^{-1}. For (a), the labels A and B denote the starting point for trajectories discussed in Fig. 13.

where u_0 is the value of the u component of the wind at the start of the trajectory. The trajectories are calculated using gridded velocity data saved every 5 min during the numerical simulation.

Of particular interest is an analysis of the forces responsible for the generation of the strong rear-inflow jet. The two trajectories presented in Fig. 13 are representative of the range of results. Each trajectory originates at 2.5 km AGL, as located on Fig. 13a, and is followed backward in time for 60 min. The path of the first trajectory (trajectory A) corresponds closely to the vertical cross section along the symmetry axis presented in Fig. 9 and represents much of the core region of the bow echo. The air parcel descends from a height of 3.5 km over the 60-min period. The integrations of the buoyancy and dynamic forcing terms along this trajectory are presented in Fig. 13b and suggest that the buoyancy terms contribute almost two-thirds of the resultant velocity. The horizontal pressure gradient associated with this term is produced almost entirely by the distribution of buoyancy within the vertical cross sections perpendicular to the bow echo. As is discussed later this portion of the rear inflow may thus be largely interpreted through the analysis of the processes that redistribute the buoyancy field in this two-dimensional vertical plane.

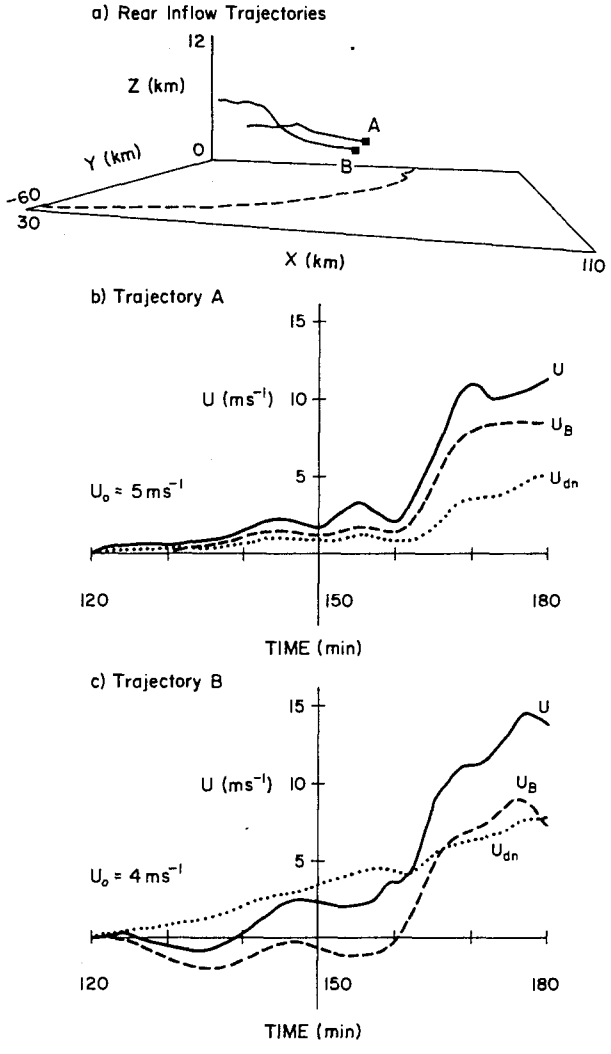

FIG. 13. Representative trajectories (a) feeding into the rear inflow at 180 min for the idealized bow echo simulation. The starting points for trajectories A and B are also indicated in Fig. 12a. The surface gust front at $t = 180$ min is denoted by the dashed line. The integration of the momentum forcing terms along trajectories A and B are presented in (b) and (c), respectively. The solid lines represent the actual magnitude of U interpolated along the trajectory, while the dashed and dotted lines represent the integrated contributions to U from the buoyancy terms (U_B) and dynamic terms (U_{dn}), respectively, as described in the text.

The second trajectory (trajectory B) is taken close to the bookend vortex. For this trajectory, the buoyancy and dynamic contributions are nearly equal (Fig. 13c). As discussed before, part of these dynamical contributions are associated with the bookend vortices. An analysis of the development of the rear inflow within this portion of the system would thus also entail an analysis of the processes producing the bookend vortex.

A similar analysis has also been completed to diagnose the forces maintaining the steady updraft along the leading edge of the bow echo. These results (not shown) reveal that much of the forcing for this updraft is due to the dynamically induced upward-directed vertical pressure gradient that is evident along the leading edge of the system in Fig. 11c. Buoyancy effects contributed only 20%–50% of the resultant updraft speeds. This result parallels a similar conclusion for supercell updrafts, whereby 60% of the updraft speed was attributable to dynamically induced vertical pressure gradients (Weisman and Klemp 1984). In the case of supercells, however, the upward-directed vertical pressure gradient is induced by a lowering of the pressure at midlevels associated with a strongly rotating updraft. For this idealized bow echo, the upward-directed vertical pressure gradient is created by the collision between the rear-inflow jet and the low-level inflow from ahead of the system. In both cases, the dynamic forcing produces a steadier circulation than if buoyancy effects were the only major contributor to updraft production.

c. Summary

During the initial two hours of this simulation, the evolution of the idealized bow echo is dominated by the splitting of the initial convective cell, as previously described, for example, by Klemp and Wilhelmson (1978b). During this period, the system-scale flow at midlevels is dominated by the development of circulations in a horizontal plane that are associated with the development of the bookend vortices. Associated with the development of the bookend vortices is a 5–10 m s^{-1} rear inflow that is strongest near the edge of the vortices. These bookend vortices remain a prom-

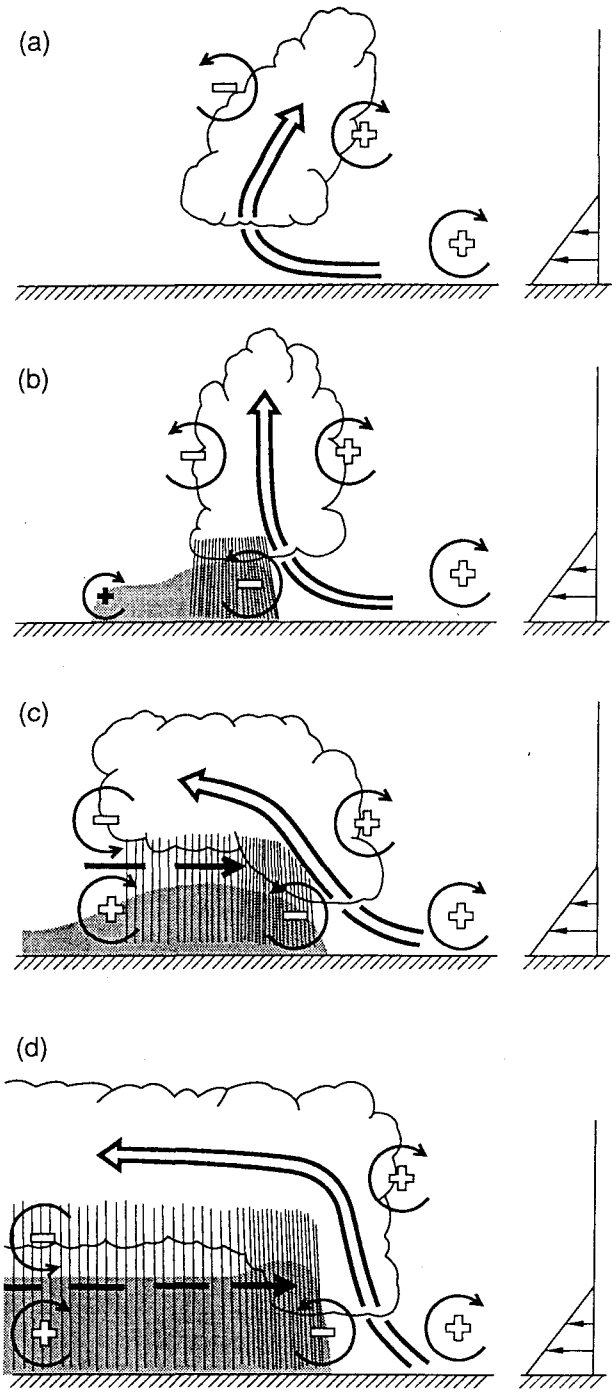

FIG. 14. Four stages in the evolution of an idealized bow echo. (a) An initial updraft leans downshear in response to the ambient vertical wind shear, which is shown on the right. (b) The circulation generated by the storm-induced cold pool balances the ambient shear, and the system becomes upright. (c) The cold pool circulation overwhelms the ambient shear, and the system tilts upshear, producing a rear-inflow jet. (d) A new steady state is achieved whereby the circulation of the cold pool is balanced by both the ambient vertical wind shear and the elevated rear-inflow jet. The updraft current is denoted by the thick double-lined flow vector, with the rear-inflow current in (c) and (d) denoted by the thick dashed vector. The shading denotes the surface cold pool. The thin, circular arrows depict the most significant sources of horizontal vorticity, which are either associated with the ambient shear or are generated within the convective system, as described in the text. Regions of lighter or heavier rainfall are indicated by the more sparsely or densely packed vertical lines, respectively. The scalloped line denotes the outline of the cloud (adapted from Weisman 1992).

inent feature of the midlevel flow through the remainder of the simulation.

As the system expands, however, a stronger vertical circulation develops in a broad zone between the bookend vortices, associated with the development of a quasi-two-dimensional updraft and elevated rear-inflow jet. As is demonstrated in the pressure analysis, the horizontal pressure gradient accelerating this rear inflow is primarily associated with a quasi-two-dimensional buoyancy-produced mesolow that extends above and behind the spreading cold pool. It is the development of this elevated rear inflow, which reaches intensities of greater than 20 m s^{-1} along the symmetry axis, that appears to be the dominant factor promoting the new steady-state structure by 180 min.

In light of this, we will proceed first with an analysis of the two-dimensional processes important to the development of this elevated rear-inflow jet and will explain how it contributes to producing an intense, steady uplift along the leading edge of the system. We will then discuss in more detail the processes promoting the development of the bookend vortices and will attempt to clarify their role in initiating and strengthening this rear-inflow circulation.

4. The development and role of the rear-inflow jet

A detailed analysis of the physical mechanisms responsible for the development of the rear-inflow jet within this simulation has recently been presented in a companion study by Weisman (1992). In this study, which extends the recent work of RKW and Lafore and Moncrieff (1989), the generation of the rear inflow is analyzed via the two-dimensional horizontal vorticity equation for inviscid Boussinesq flow; for example,

$$\frac{d\eta}{dt} = -\frac{\partial B}{\partial x}, \tag{8}$$

where $\eta = \partial u/\partial z - \partial w/\partial x$ and where B represents the buoyancy, defined by (2). Within this framework, the only source of horizontal vorticity is horizontal gradients of buoyancy. Thus, the analysis of the development of circulation is simplified to understanding the evolution of the buoyancy field.

This perspective allows for a simple interpretation of the evolution of quasi-two-dimensional convective systems, based on the interactions between the buoyant updraft, the storm-induced cold pool, and the ambient vertical wind shear. This evolution is presented schematically in Fig. 14 for an isolated cell evolving in a vertically sheared environmental flow. Initially, the convective cell leans downshear in response to the am-

bient vertical wind shear (Fig. 14a). As a cold pool develops beneath the convection, the horizontal buoyancy gradients along the edge of the cold pool generate circulation that, along the downshear edge of the cold pool, is of the opposite sense as the circulation inherent in the ambient shear. When this cold pool circulation balances the circulation inherent in the ambient shear, deeper lifting is produced at the cold pool edge, resulting in stronger, more upright convective cells (Fig. 14b). As the cold pool circulation continues to strengthen, it eventually overwhelms the ambient shear, and the convective circulation begins to tilt rearward over the cold air (Fig. 14c).

It is during this upshear-tilting phase of the system that a significant rear-inflow jet is characteristically generated. This occurs as the horizontal buoyancy gradients along the rear edge of the buoyant plume aloft and cold pool near the surface generate horizontal vorticity, thereby accelerating the flow from rear to front at midlevels (as indicated in Fig. 14c by the bold arrow between the positive and negative circulation couplet at the back edge of the system). This mechanism is equivalent to that described via the diagnostic pressure analysis (section 3c) in that this configuration of the buoyancy field also implies a minimum in the buoyancy-derived pressure field at midlevels that accelerates the rear-inflow current.

For the idealized bow echo, the transition to an upshear-tilted circulation occurs shortly after 120 min. Over the next 60 min, the rear inflow along and near the symmetry axis accelerates from 5 to 20 m s^{-1}. As described by RKW, this upshear-tilting phase often denotes the beginning of the decay stage of the convective system, as the lifting along the leading edge of the gust front becomes shallower than during the earlier phases of system evolution (due to the dominating influence of the cold pool). However, this tendency toward decay can be superseded by the development of an elevated rear-inflow jet, as is presented schematically in Fig. 14d (Weisman 1992). In this scenario, the rear-inflow jet is characterized by the opposite sense of horizontal vorticity beneath the jet level as is generated by the cold pool, and may thereby counteract some of the negative influence of the cold pool circulation. For the idealized bow echo, the strength of the horizontal vorticity beneath this elevated jet is sufficient to again promote deep lifting at the leading edge of the gust front, leading to the continual regeneration of strong erect updrafts at that location. It is this forced lifting, promoted by the development of the strong, elevated rear-inflow jet, that appears to be the primary factor promoting the strength and longevity of this idealized bow echo.

Once the updraft air is lifted above the level of the rear-inflow jet, it is drawn rapidly rearward above the cold pool under the influence of the horizontal vorticity associated with the upper portion of the jet. Thus, while the low-to-midlevel updrafts during this phase in the systems life are actually stronger than at earlier times, the updraft at higher levels is weaker, and the convective cells shallower. This explains why the updraft trajectories at the core of the bow echo in Fig. 10 are shallower than for the more isolated cells along the periphery of the system.

As described by Weisman (1992), the environmental conditions conducive to the development of strong, elevated rear-inflow jets include both large amounts of CAPE and strong low-level vertical wind shear. These conditions are necessary in that the development of an elevated rear-inflow requires the production of a strongly buoyant plume of air within the updraft current spreading rearward above the cold pool. The CAPE is important in this regard in that it ultimately controls the maximum potential temperature excess that can be realized within a parcel of air rising within the updraft. The vertical wind shear is additionally important in that potential temperature excesses within the updraft current are maximized when near-surface air is lifted quickly to its level of maximum buoyancy, thereby reducing the mixing along the parcel's path. As discussed previously, the strongest lifting of near-surface air is produced when there is strong low-level vertical wind shear to help balance the cold pool–generated circulation. If the contributions to the generation of the rear-inflow jet due to the warm plume of air aloft are similar in magnitude to the contributions due to the cold pool near the surface, then the rear-inflow jet may remain elevated to near the leading edge of the system. However, if the contributions from the cold pool are significantly larger than those from the warm plume aloft, then the rear-inflow jet descends and spreads along the surface well behind the leading edge of the gust front, leading to a shallower, weaker system-scale circulation. These environmental constraints on the production of long-lived bow echoes are discussed in more detail in section 6.

5. The origin and role of the bookend vortices

The goal of this section is to trace the source of the bookend vortices and to discern what role they might play in the initiation and enhancement of the bow echo circulation. This analysis is guided by the three-dimensional vorticity equation for inviscid Boussinesq motion:

$$\frac{d\boldsymbol{\omega}}{dt} = \boldsymbol{\omega}\cdot\nabla\mathbf{v} + \nabla\times(B\mathbf{k}), \tag{9}$$

where $\boldsymbol{\omega}$ is the vorticity vector and B represents the buoyancy field, as defined by (2). The first term on the right represents the effects of tilting and stretching, which alter an existing vorticity field, while the second term represents the generation of horizontal components of vorticity by horizontal gradients in the buoyancy field. In describing the evolution of the bookend vortices, we will be especially interested in the vertical

component of the vorticity equation, which is given by

$$\frac{d\zeta}{dt} = \boldsymbol{\omega}_H \cdot \nabla_H w + \zeta \frac{\partial w}{\partial z}, \qquad (10)$$

where $\boldsymbol{\omega}_H$ represents the horizontal components of the vorticity vector, $\zeta = \partial v/\partial x - \partial u/\partial y$ is the vertical component of vorticity, and the first and second terms on the right represent the usual tilting and stretching effects, respectively.

a. The origin of the bookend vortices

In a horizontally homogeneous nonrotating fluid, vertical vorticity is generated by tilting the horizontal vorticity $\boldsymbol{\omega}_H$ inherent in the ambient flow. For example, an isolated updraft growing in a vertically sheared environment will deform the horizontal vortex lines inherent in the ambient shear upward, producing cyclonic and anticyclonic vortices on the flanks of the cell (Fig. 15a). Once vertical vorticity is created, then the stretching terms may act to either increase or decrease the existing vorticity. The subsequent development of a downdraft will deform this pattern considerably as the downdraft gradients provide an additional source of tilting and the downdraft accelerations stretch the vertical vorticity previously produced by the updraft. In conditions of sufficiently strong environmental vertical wind shear and CAPE, cell splitting may occur, resulting in two mirror-image storms with the right member of the splitting pair consisting of a cyclonic updraft and anticyclonic downdraft at midlevels and the left member consisting of an anticyclonic updraft and cyclonic downdraft (Fig. 15b). This process is recognized as fundamental to the development of supercell storms (e.g., Klemp 1987).

The initial evolution of the vertical vorticity field for the idealized bow echo corresponds closely to this simple model. Between 60 and 120 min, the initial cell splits into right- and left-moving cells, with the right-moving cell exhibiting a cyclonic updraft and anticyclonic downdraft, etc. Figure 16 displays the system-relative flow and θ_e at 2.5 km AGL at 90 min, when the split cell has become well established. A series of vortex lines emanating from the bookend vortex, as located in Fig. 16a, is presented in Fig. 16b. At this time, most of the vortex lines originate in the ambient shear layer to the south of the storm, and are tilted upward and downward as they encounter the updraft–downdraft couplet. The location of the anticyclonic vortex on the gradient between high and low θ_e is consistent with the conservation of equivalent potential vorticity, as discussed by Rotunno and Klemp (1985). Since the θ_e surfaces and ambient vortex lines are both oriented horizontally in the initial state, the ambient vortex lines will continue to lie within the original θ_e surfaces as the flow evolves (assuming no mixing), and they will both be deformed similarly by the updrafts and downdrafts. This results in the ambient vortex lines tilting vertically through zones of horizontal gradients of θ_e, producing the observed vertical vorticity pattern.

As the system expands, the original split updraft is replaced by a quasi-two-dimensional line of updrafts extending along the leading edge of the gust front. As a result, the well-defined cyclonic eddy coincident with the updraft at 90 min is not evident at later times, although regions of weaker cyclonic vorticity are still produced within the new, more short-lived updrafts generated along the spreading outflow. However, the bookend vortex that originates in the splitting downdraft is prominent throughout this process. Figure 17 presents this structure at 180 min, when the system has evolved into the quasi-steady bow echo. Although the bookend vortex is again located within the horizontal gradients of θ_e, only the warm side of the vortex is now associated with vortex lines that originated in the ambient shear layer. The remaining vortex lines circle back toward the core of the bow echo, producing a three-dimensional vortex ring centered on the elevated rear-inflow jet.

Figure 18 more clearly depicts the association between the vertical vorticity field at 2.5 km AGL and the vertical velocity field, along with calculations of the standard tilting and stretching terms as defined in (10). At 90 min, the region of positive vertical vorticity is well correlated with the region of strongest updraft, while the region of negative vertical vorticity is located on the gradient between the updraft and downdraft, although mostly within the downdraft (Fig. 18a). The tilting term is the primary contributor to the positive vorticity within the updraft at this height (Fig. 18b), with weaker contributions from the stretching terms. For the downdraft region, the tilting contributions to the negative vertical vorticity are much weaker, with the primary contributions now comming from the stretching terms. An analysis in which the vorticity forcing terms are integrated along parcel trajectories (not shown) confirms that the relative magnitude of the forcing depicted in the horizontal cross sections is also representative of the relative integrated forcing contributions.

By 180 min, the zone of negative vorticity associated with the bookend vortex has increased substantially in size, although the maximum magnitude of the vorticity has decreased (Fig. 18d). The positive vorticity associated with the updrafts is also much weaker, with the stretching and tilting terms also displaying similar but weaker contributions to the vorticity field than earlier (Fig. 18e, f). Small zones of more intense vorticity and vorticity forcing are evident behind the leading edge of the updraft, closer to the symmetry axis, but these features are transitory and are not considered further.

The source of the vertical vorticity for the bookend vortex can be clarified further through a direct application of the circulation theorem; for example, Rotunno and Klemp (1985):

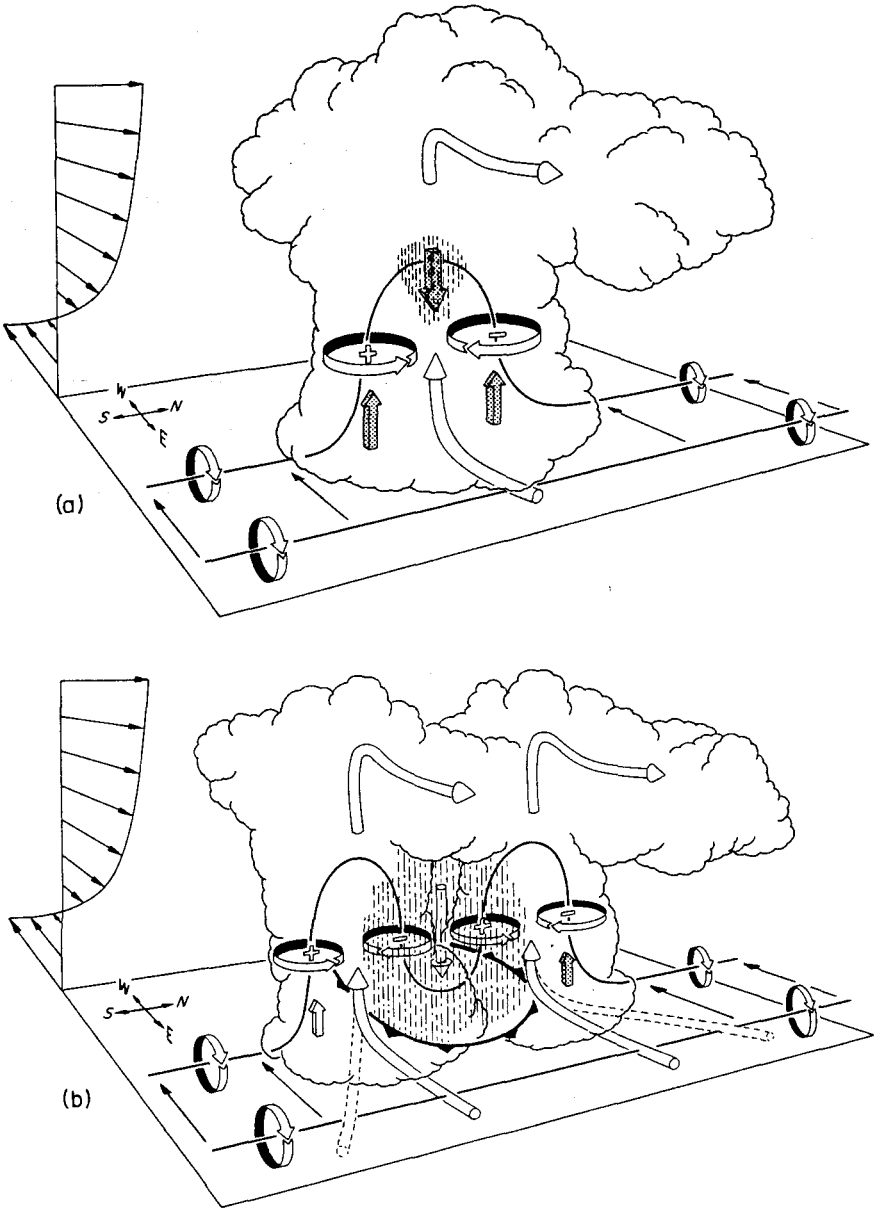

FIG. 15. Schematic depicting how a typical vortex tube contained within (westerly) environmental shear is deformed as it interacts with a convective cell (viewed from the southeast). Cylindrical arrows show the direction of cloud-relative airflow, and heavy solid lines represent vortex lines with the sense of rotation indicated by circular arrows. Shaded arrows represent the forcing influences that promote new updraft and downdraft growth. Vertical dashed lines denote regions of precipitation. (a) Initial stage: vortex tube loops into the vertical as it is swept into the updraft. (b) Splitting stage: downdraft forming between the splitting updraft cell tilts vortex tubes downward, producing two vortex pairs. The barbed line at the surface marks the boundary of the cold air spreading out beneath the storm (from Klemp 1987).

$$\frac{dC}{dt} = \int_C B\mathbf{k} \cdot d\mathbf{l}, \tag{11}$$

where the circulation C is defined as

$$C \equiv \int_C \mathbf{v} \cdot d\mathbf{l} = \int_S (\nabla \times \mathbf{v}) \cdot d\mathbf{A} \tag{12}$$

and the integration is taken about any closed circuit C on a given surface S. Following the approach of Rotunno and Klemp (1985), a series of closed circuits have been specified that encompass the bookend vortices for a sequence of times between 120 and 240 min. Each circuit is traced backward in time by calculating time-dependent parcel trajectories at 1-km intervals

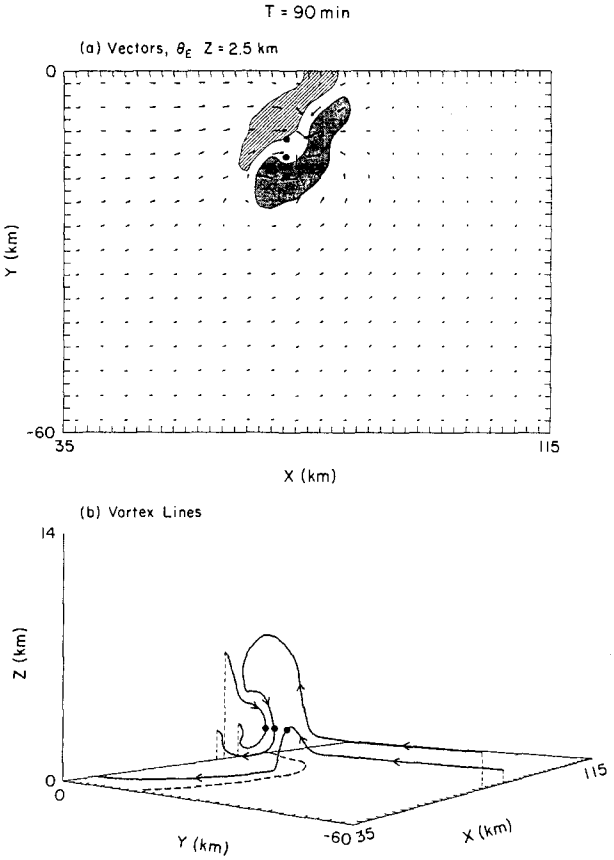

FIG. 16. Bookend vortex structure at t = 90 min for the idealized bow echo. (a) Horizontal cross section of flow vectors and θ_e at 2.5 km AGL. Vectors are presented at every other grid point, with a vector length of two grid points representing a magnitude of 25 m s^{-1}. A domain speed of u = 22.5 m s^{-1} has been subtracted from the flow field. The ground-relative system propagation speed at this time is 22 m s^{-1}. θ_e greater than 332 K is darkly shaded, while θ_e less than 326 K is lightly shaded. (b) Vortex lines traced from the locations within the bookend vortex denoted by the dots in (a). The sense of the vorticity vector is indicated by the arrows. The thick dashed line denotes the location of the surface gust front.

around the circuit using data saved every 5 min. The circulation and the circulation forcing, as defined by (11) and (12), is then calculated at 100-sec intervals for each circuit through the analysis period. In the absence of horizontal vorticity generation and mixing effects, the circulation about the circuit will be conserved, and the source of the vertical vorticity must be traced ultimately to the tilting of horizontal vorticity inherent in the ambient shear. If horizontal vorticity is generated along a vertical portion of the circuit over the analysis period, then the circulation will not be conserved and should change at the rate specified by the circulation forcing term. In general, the circuits remained well defined for about 20 min prior to each analysis time, as mixing effects (both physical and numerical) began to dominate beyond this period. However, 20 min was sufficient to clearly identify the source region for the air parcels making up each circuit and thereby offers some insights into the source for the circulation as well.

The range of results is well represented by the analysis of the bookend vortex circuit that is specified at 180 min, as identified by the rectangle in Fig. 17. The history for this circuit is presented in Fig. 19. The air parcels that are incorporated into the circuit originate primarily from two sources. One set of air parcels (located between B and C on the figure) originates near the surface, ahead of the system, and is characterized by high values of θ_e. Another set of air parcels (located between A and D on the figure) originates in the 3–5-km layer to the rear of the system and descends in conjunction with the rear-inflow jet. These air parcels are characterized by low values of θ_e.

A time series of the circulation along with the integrated contributions from the circulation forcing term for this circuit are presented in Fig. 20. This analysis suggests that the circulation increased in strength by 30% during the prior 20 min (solid line), with the integrated forcing (dashed line) contributing much of the observed variation. This would suggest that horizontal vorticity generated within the convective system may have contributed significantly to the strength of

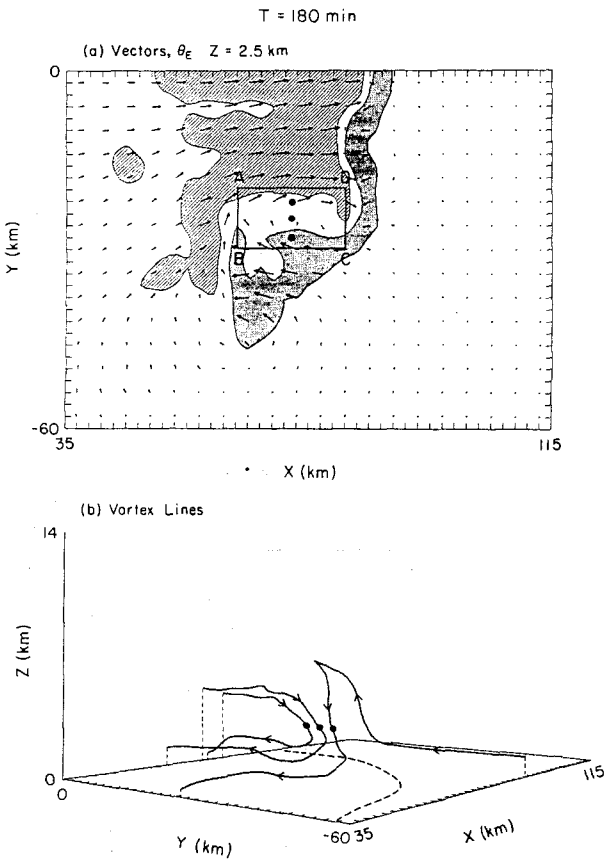

FIG. 17. Same as Fig. 16 but at t = 180 min. The ground-relative system propagation speed at this time is 27 m s^{-1}. The box in (a) denotes the location of a circuit that is followed over time in Fig. 19.

the bookend vortices at 180 min. For instance, such horizontal vorticity generation is largely responsible for the development of the strong rear-inflow jet, as discussed in section 4. The question arises, however, as to how such horizontal vorticity could be tilted systematically to produce the bookend vortex feature.

One scenario in which convectively generated horizontal vorticity might contribute systematically to the production of the bookend vortex is if air parcels flowing into the vortex traveled along a horizontal buoyancy gradient while they ascended or descended into the vortex. Thus, horizontal vorticity that is generated along the parcels' path could be systematically tilted to contribute to the vortex. This concept of the generation of streamwise vorticity has been used, for example, to explain the preferential development of low-level rotation within supercell updrafts (e.g., Rotunno and Klemp 1985).

In the present scenario, the only parcel paths that could be identified that could contribute in the proper sense to the development of the bookend vortex were those parcels that started near the surface ahead of the system and that traveled along and then over the southern, curved portion of the cold pool before descending into the vortex (e.g., parcels between points B and C in Fig. 19). Further analysis, however, failed to confirm this as a significant vorticity source for the vortex. Thus, a more careful analysis may be needed to clarify the role of the convectively generated horizontal vorticity in producing the bookend vortex structure. All in all, the most significant signal from this analysis is the relative conservation of the circulation for the circuit over the 20-min period, suggesting that tilting and subsequent stretching of the horizontal vorticity inherent in the ambient vertical wind shear is the primary contributor to the production of the bookend vortices. This hypothesis is supported further in section 6, where we note that significant bookend vortices are produced only in simulations in which the ambient vertical wind shear is of at least moderate strength (thereby supplying a continual, significant source of horizontal vorticity to be tilted and stretched).

b. The role of the bookend vortices

Since the source for the bookend vortex circulation is largely distinct from that producing the two-dimensional vertical circulation described in section 4, one might ask what the relative role of these vortices is in producing the steady-state bow echo structure. For this purpose, it is useful to draw an analogy between the bookend vortices and idealized, two-dimensional vortex couplets. A schematic representing the basic properties of a vortex couplet is presented in Fig. 21. The velocity field of the couplet may be interpreted as the vector sum of the velocity field induced by each vortex individually. The net flow field includes a jet of air between the two vortices (where the two flow fields add) and much weaker flow outside the vortices (where the flow fields subtract). The enhancement of the flow between the vortices can be interpreted as a focusing effect of the vortex couplet. The pressure field is characterized by pressure deficits coincident with the vortices, which are dynamically balanced with the rotating flow, and a zone of slightly lowered pressure extending between the vortices, which produces a pressure gradient that is consistent with the acceleration of the flow between the vortices. This configuration is qualitatively similar to the flow and dynamic pressure pattern presented at 180 min for the idealized bow echo (e.g., Figs. 12 and 18d).

A vortex couplet propagates as the flow field induced by each vortex advects the other along. The motion of the vortex couplet and the strength of the jet depends on the prescribed sizes and magnitudes of the vortices as well as the spacing between them. By comparing the flow field of vortex couplets of various sizes and magnitudes to the flow field realized in the full bow-echo simulation, we can estimate to what extent the bookend vortices contribute to the overall circulation.

For this purpose, we employ a simple time-dependent two-dimensional vortex model, as described in the Appendix. The bookend vortices depicted in the simulation are approximated by placing two circular regions of vorticity having opposite signs at various distances apart. The radius of each vortex is set at 7 km, roughly approximating the mean size of the vortices between 120 and 240 min in the idealized simulation, with the vorticity within each vortex increasing smoothly to a maximum in the center. Note that the size of the vortex is defined by the size of the region of significant vertical vorticity rather than the size of the apparent region of circulation, which may be much larger (e.g., Fig. 18d). The spacing between the vortices is varied between 20 and 60 km, with the maximum magnitude of the vorticity ranging up to 0.015 s^{-1}. The resolution of the vortex model is set at 2 km, to compare directly with the full simulation.

Figure 22 depicts the magnitude of the jet induced on the axis between the idealized vortices for the specified range of conditions. Also presented is the approximate magnitude and spacing of the bookend vortices along with the observed rear-inflow strength on the symmetry axis at 2.5 km AGL, presented every 30 min between 150 and 240 min, for the full simulation. These results suggest that an idealized, two-dimensional vortex couplet with the characteristics of the bookend vortices would induce between 7 and 12 m s^{-1} of rear inflow on the symmetry axis. This represents 40%–50% of the observed strength of the rear inflow at the analysis times. Since the analogy between the bookend vortices and an idealized vortex couplet is at best qualitative, these results must be viewed with some caution. However, trajectory calculations as presented in section 3b suggest that nearly 30% of the acceleration of the rear-inflow jet near the symmetry axis of the simulation is

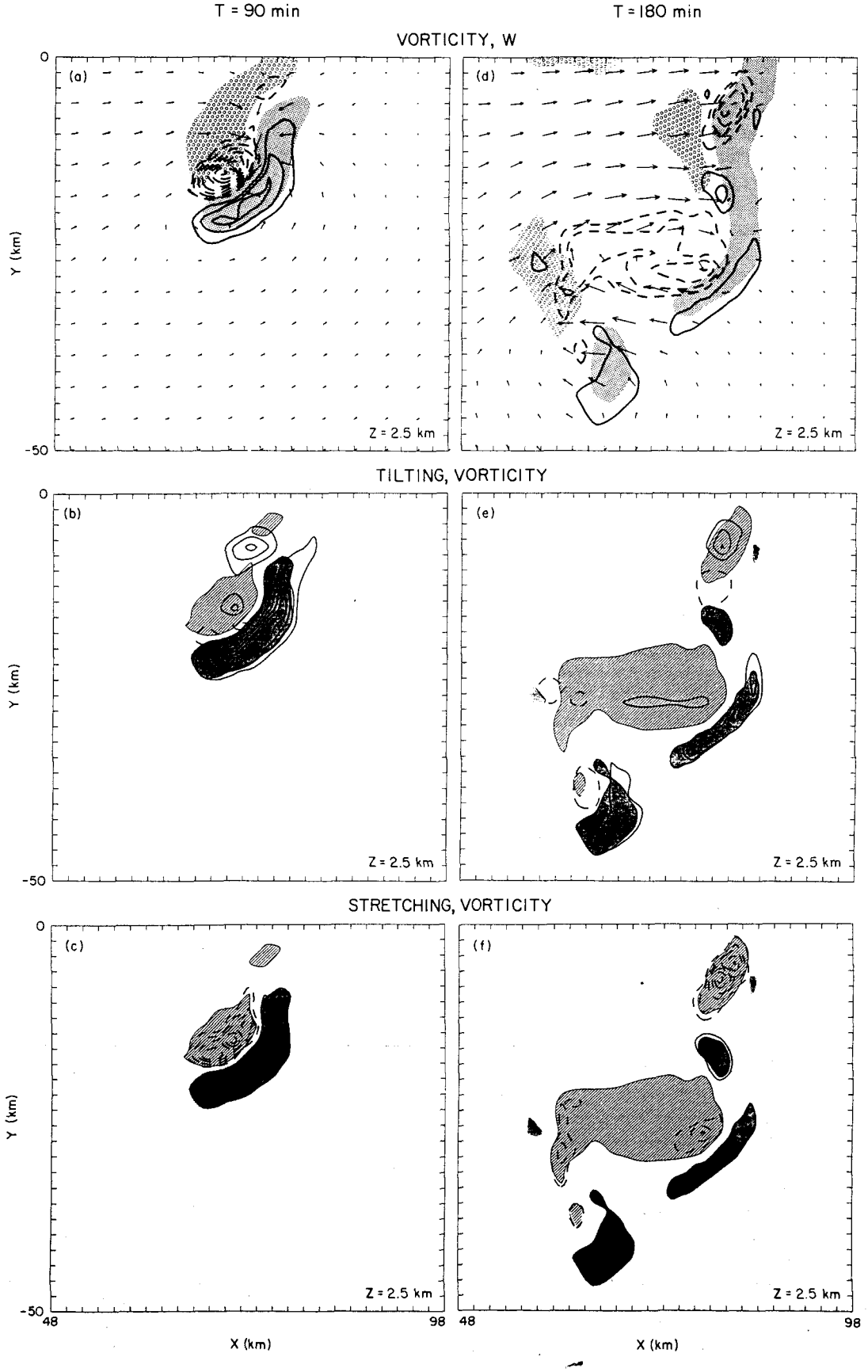
T = 90 min
T = 180 min
VORTICITY, W
(a)
(d)
TILTING, VORTICITY
(b)
(e)
STRETCHING, VORTICITY
(c)
(f)
Z = 2.5 km
Y (km)
X (km)
0
-50
48
98

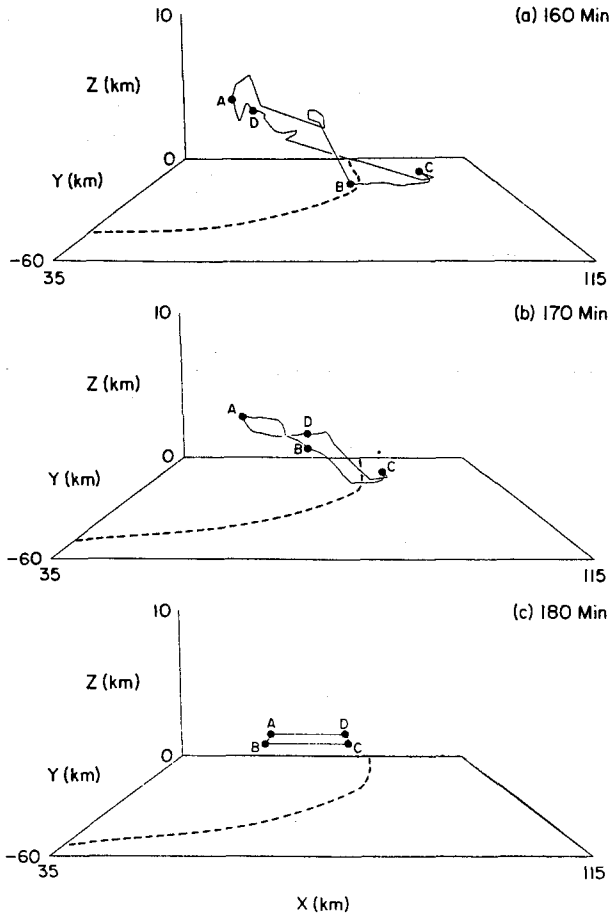

FIG. 19. Evolution of the bookend vortex circuit depicted in Fig. 17, ending at t = 180 min. The circuit is traced at (a) 160 min, (b) 170 min, and (c) 180 min, with the corner points of the circuit, labeled A, B, C, and D, marked at each time for reference. The sense of the circuit is positive in the counterclockwise direction. The thick dashed line denotes the location of the surface gust front.

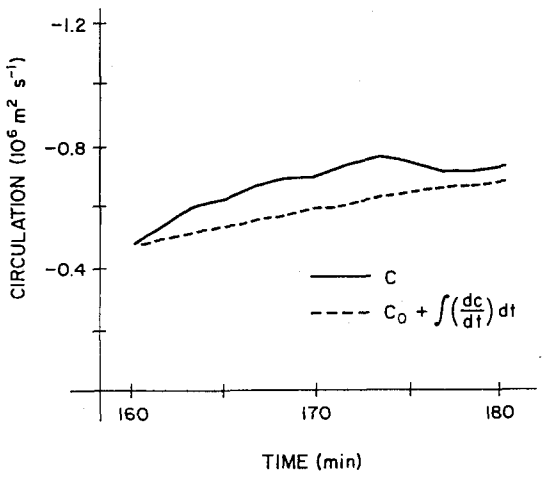

FIG. 20. Time series of circulation (solid) and integrated circulation forcing (dashed) for the circuit described in Fig. 19, which is followed from 160 through 180 min.

associated with dynamically induced horizontal pressure gradients, with these contributions increasing to nearly 50% along the flanks of the system. A significant portion of this dynamical pressure gradient appears to be associated with the bookend vortices. This suggests that the bookend vortices do play a significant role in enhancing the strength of the bow-echo circulation.

A similar analysis of the induced propagation speeds for these idealized vortex rings (not shown) suggest magnitudes of only 2 m s^{-1}. The propagation speeds for the full bow echo, however, range between 25 and 30 m s^{-1}. Thus, the propagation that might be induced by the bookend vortices does not appear to contribute significantly to the system motion.

6. Environmental conditions for bow-echo genesis

The hypotheses put forth in the preceding sections to explain the development of the idealized bow echo depend on both the strength of the low-level vertical wind shear and the amount of thermodynamic instability in the environment ahead of the system. The vertical wind shear controls the characteristics of the lifting that is realized at the leading edge of the gust front as well as the ability to generate the bookend vortices at the edges of the system. The thermodynamic instability, however, controls ultimately the maximum amount of buoyancy that can be realized within the updraft current that spreads rearward above the surface cold pool, which is a crucial factor in the development of a strong, elevated rear-inflow jet. This suggests that convective systems with characteristics similar to the idealized bow echo can exist for a rather wide range of ambient thermodynamic and vertical wind-shear conditions, as long as certain minimum thresholds for each of these environmental parameters is achieved. The goal of this section is to more clearly establish what these thresholds are for the idealized simulations and to compare these results to the environmental conditions associated with observed severe, long-lived bow echoes.

FIG. 18. Horizontal cross sections at 2.5 km AGL depicting vertical vorticity, tilting, and stretching, along with vertical velocity and flow vectors at [(a), (b), and (c)] 90 min and [(d), (e), and (f)] 180 min. For (a) and (d), vertical vorticity is contoured every 20 × 10^{-4} s^{-1}, with regions of vertical velocity greater than 4 m s^{-1} darkly stippled and regions of vertical velocity less than −2 m s^{-1} lightly stippled. Vectors are presented every other grid point, with a vector length of two grid points representing a magnitude of 25 m s^{-1}. A domain speed of 22.5 m s^{-1} has been subtracted from the flow field. For (b), (c), (e), and (f), the tilting and stretching terms are contoured every 8 × 10^{-6} s^{-2}, respectively, with regions of vertical vorticity greater than 20 × 10^{-4} s^{-1} darkly shaded and vertical vorticity less than −20 × 10^{-4} s^{-1} lightly shaded. The zero contour is omitted.

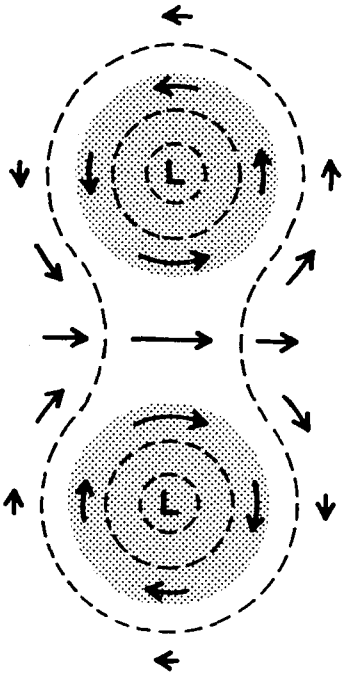

FIG. 21. Schematic representation of an idealized two-dimensional vortex couplet, depicting the stronger flow induced between the vortices. Shading denotes regions of constant vorticity. Unshaded regions have zero vorticity. Dashed contours represent an approximate negative pressure perturbation field that is consistent with the flow pattern. The L denote the locations of the lowest pressure.

For this purpose, the ambient wind and thermodynamic profiles are varied over a wide range of conditions associated with severe convective systems. The thermodynamic profile is varied by changing both the lapse rate through the troposphere, as depicted in Fig. 3, and the low-level mixing ratio. This produces variations in the CAPE, level of free convection (LFC), and the amount of negative area to be overcome by a rising parcel. The range of conditions covered by these experiments is presented in Table 1, and includes the range of observed conditions associated with bow-echo events. Two different wind-shear profiles are also considered. The first restricts the shear layer to the lowest 2.5 km AGL with constant winds above, as for the simulations discussed previously. The second extends the shear layer to 5 km AGL. Each shear profile is varied in magnitude from $U_s = 5$ m s^{-1} to $U_s = 40$ m s^{-1} for the maximum wind over the prescribed depth. As before, a single cell is initialized on the symmetry axis of the model domain and is allowed to evolve through 240 min of simulation time.

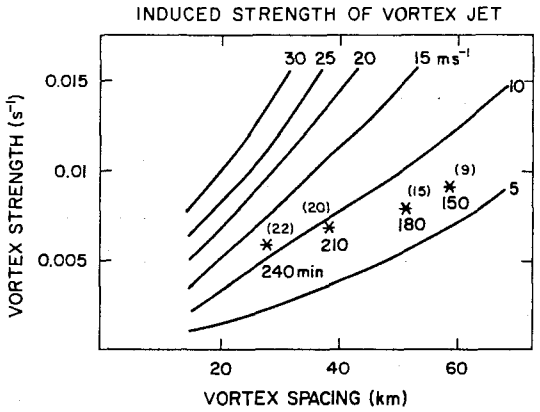

FIG. 22. Induced strength of the jet between the vortices for an idealized two-dimensional vortex couplet, given the spacing between the vortices and the strength of the vortices. The observed strength of the bookend vortices at 150, 180, 210, and 240 min for the idealized bow echo are included in the figure, along with the observed strength of the rear-inflow jet between the vortices at those times (numbers in parentheses, meters per second, taken relative to the ambient 2.5-km flow).

a. *Simulation results*

Three basic types of convective organization are identified in these experiments, as depicted schematically in Fig. 23. The first category, designated "W," consists of cases in which the cold pool circulation clearly overwhelms the ambient vertical shear. This leads to an upshear-tilted system of rain cells tens of kilometers behind the leading edge of the gust front. These systems characteristically develop strong rearward flow above the cold pool, with only weaker, disorganized midlevel rear inflow into isolated cells at the back edge of the system. The rear inflow descends quickly to the ground to produce a wide zone of system-relative surface outflow extending to the leading edge of the gust front. Portions of these systems may appear bow shaped for short periods of time and may also produce periods of strong surface winds (especially early in the evolution, in association with strong, isolated convective cells), but these features tend to dissipate quickly, and the structures described for the idealized long-lived bow echo (e.g., an elevated rear-inflow jet and bookend vortices) do not develop. An example of this evolution is the moderate-shear case described by Weisman (1992).

A second category, designated "B," represents cases that develop a long-lived bow echo structure, similar

TABLE 1. Thermodynamic conditions used for environmental sensitivity experiments.

CASE	Low-level mixing ratio (g kg^{-1})	Cloud base (m)	Level of free convection (m)	CAPE (m^2 s^{-2}) Negative	CAPE (m^2 s^{-2}) Positive
1	14	1107	1907	−17	1182
2	13	1252	1952	−16	1795
3	14	1107	1707	−12	2377
4	15	963	1363	−5	3011
5	13	1252	1752	−10	3187
6	14	1107	1507	−6	3847
7	15	963	1263	−2	4549

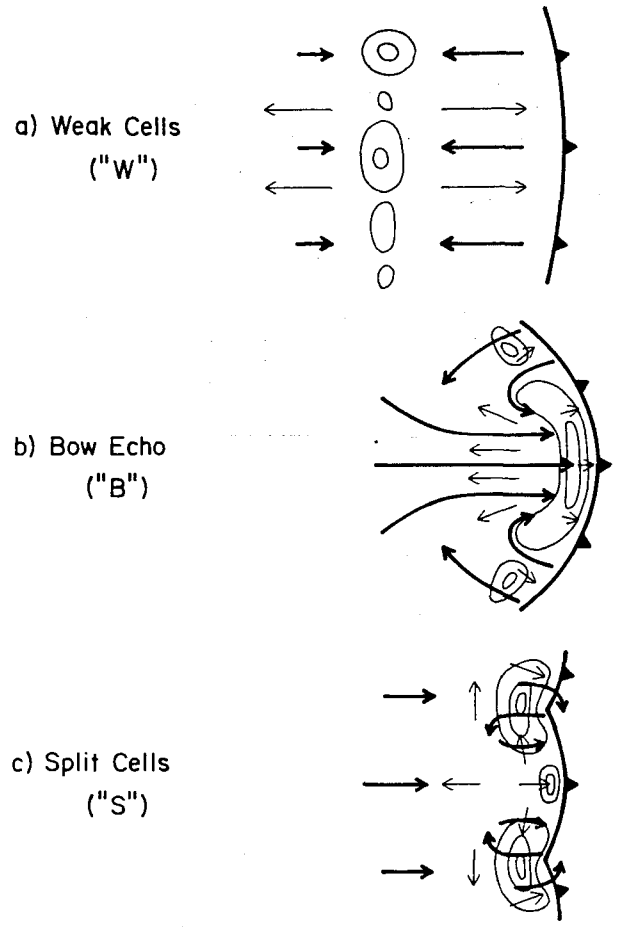

FIG. 23. Schematic depiction of the primary modes of convective organization identified in the sensitivity experiments between 180 and 240 min. Thick and thin arrows represent system-relative flow at 2.5 km AGL and the surface, respectively. Contours represent rainwater concentration. Thick barbed line represents the location of the surface gust front.

to that described for the idealized experiment. Such cases are characterized by a 40–80-km bow-shaped arc of rain cells along the leading edge of the system. A strong, elevated rear-inflow jet extends to the leading edge of the gust front, with strong rearward flow at the ends of the bow forming bookend vortices. Strong system-relative surface outflow is confined to a narrow (5–10-km) zone just behind the gust front. An intermediate category, designated "I," represents cases that have attributes of both cases W and B (not included in Fig. 23).

A third category, designated "S," is characterized by strong, more isolated, long-lived cells scattered along the leading edge of the gust front. Many of these cells are supercellular, consisting of rotating updrafts and having evolved through a splitting process. Each cell may induce strong, midlevel jet features associated with cell-scale processes, but a larger-scale organized rear inflow, as occurs with the idealized bow echo, is not evident.

The form of organization that dominates these simulations between 180 and 240 min is depicted in Fig. 24. The cases with $U_s = 15$ m s^{-1} or less over the prescribed depth all evolve as described for the disorganized systems, independent of the amount of instability. As the shear increases, more organized structures occur, with bow echoes dominating the stronger-instability part of the range and split supercells favored for the weaker-instability cases or the strongest deep-shear cases. Recall, however, that the cases that eventually evolve into bow echoes all originate with splitting cells earlier in the lifetime of the system, as described for the idealized bow echo discussed earlier. It is possible that some of the supercell cases at 240 min could also evolve into bow echo structures at later times if the cold pools continue to strengthen and deepen. As the depth of the shear layer increases, the range of conditions that produce bow echoes shrinks to the higher-instability, intermediate-shear range of the spectrum. In general, well-defined, long-lived bow echoes occur

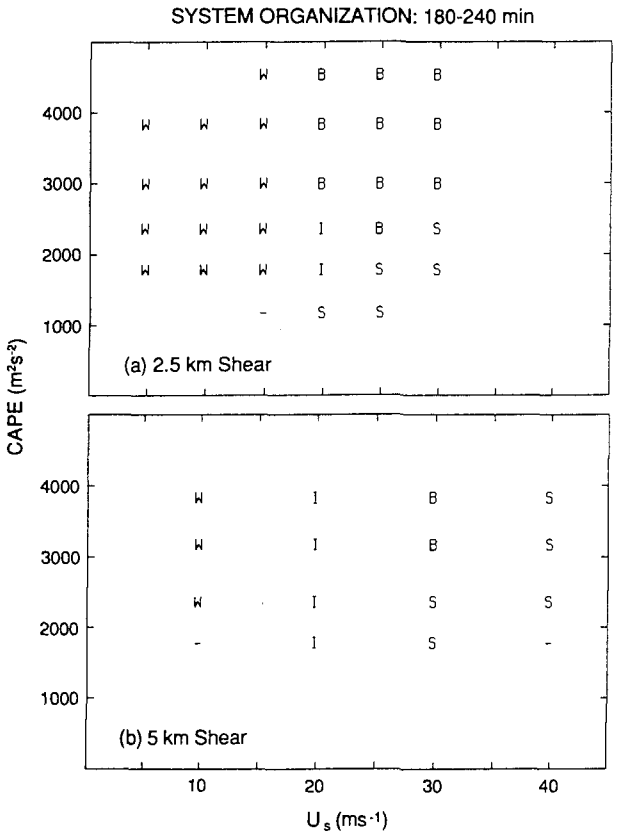

FIG. 24. Primary modes of convective organization identified for the (a) 2.5-km shear and (b) 5-km shear experiments between 180 and 240 min for each simulation. U_s represents the maximum magnitude of the wind for each wind profile. In the figure W represents a weak upshear-tilted system, I represents an intermediate form of organization, B represents a bow echo, and S represents split supercells, as described in Fig. 23 and in the text; "–" indicates that the storm system had dissipated by 180 min.

for shear magnitudes of at least 20 m s^{-1} over the prescribed depth and CAPEs of at least 2200 m^2 s^{-1}. In retrospect, the idealized bow echo case represents about the minimum CAPE that produces this type of convective structure within these simulations.

One of the more pertinent characteristics of bow echoes and, indeed, the one that created much of the observational interest is their propensity to produce long swaths of damaging surface winds. Figure 25 presents the maximum ground-relative wind realized at the lowest level of the model (350 m) at 240 min for each simulation. The strongest winds at 240 min generally occur for both stronger shears and stronger CAPE. If we consider maximum 350-m winds of 35 m s^{-1} or greater as indicating significant potential for producing damaging surface winds, then we note that such systems occur for all cases of CAPE greater than 2000 m^2 s^{-2} and shears greater than 15 m s^{-1}, including but not restricted to the cases that have evolved into structures similar to the idealized bow echo. Since a free-slip condition has been specified at the lower boundary, these model-produced near-surface winds may be a slight overestimate of the actual surface wind speeds that would be observed in such systems. However, the inclusion of surface drag in such simulations (e.g., Wilhelmson and Chen 1982) does not significantly effect the overall system evolution, suggesting that the general dependence of near-surface wind magnitudes on environmental vertical wind shear and CAPE would also remain intact. Future studies, though, must more carefully consider these effects.

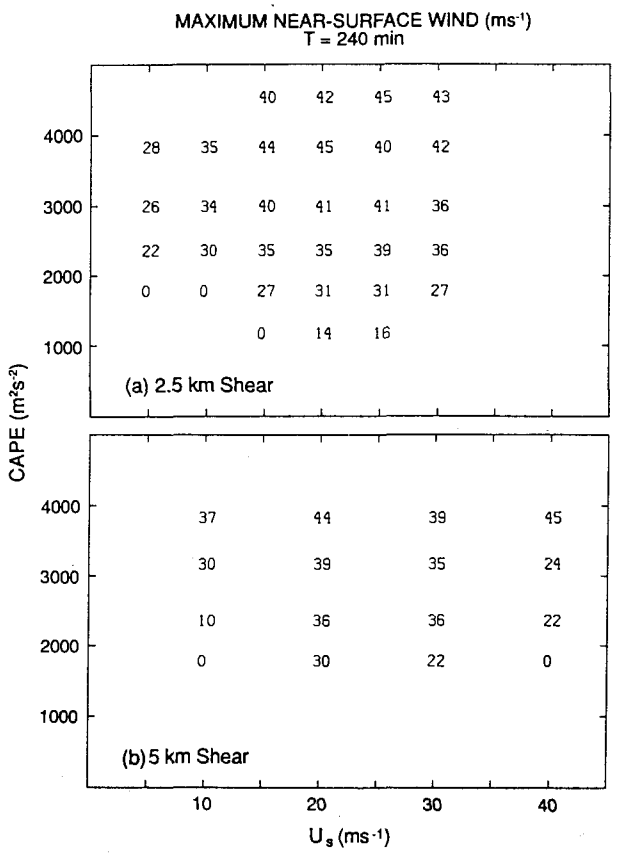

FIG. 25. Maximum near-surface (350 m AGL) wind (m s^{-1}) for the (a) 2.5-km shear and (b) 5-km shear experiments at t = 240 min. U_s represents the maximum magnitude of the wind for each wind profile.

b. *Comparison with observations*

A qualitative comparison between these model-derived criteria and the results from the observational cases discussed in the Introduction suggests many similarities. For instance, both the present study and the derecho climatology clearly indicate that large amounts of instability and moderate-to-strong magnitudes of environmental vertical wind shear are necessary for such severe, long-lived wind events. However, the minimum magnitude of the wind shear for the observed derechos is slightly less than that for the simulated bow echoes; that is, at least 15 m s^{-1} of speed variation from the surface to 700 mb was observed for the derechos, while a 20 m s^{-1} threshold was suggested for the long-lived, idealized bow echoes. This apparent discrepancy, though, may merely reflect the observational tendency to identify derecho events based on surface winds alone, rather than on the long-lived structural characteristics emphasized in the present study. As discussed before, if the present simulations are categorized based on surface winds alone, then the minimal vertical shear conditions for the production of long-lived convective systems with strong surface winds does decrease to the 15 m s^{-1} of low-level wind variation noted for the derechos. This suggests that a variety of mesoconvective structures can be associated with long-lived, damaging surface wind events, with the idealized bow echo described herein representing an extreme example that occurs only for the stronger-shear cases.

As a more specific example from the Introduction, the 28 May case described by Burgess and Smull (1990) exhibits 4200 m^2 s^{-2} of CAPE with about 17 m s^{-1} of shear over the lowest 2 km AGL, extending in a more complicated fashion over greater depths. These environmental conditions fall well within the range of conditions that produce severe near-surface winds within the simulations, but the vertical shear magnitudes are more characteristic of the intermediate category of convective structures rather than of the long-lived bow echoes. Consistently, this particular convective system evolves much more quickly than the idealized bow echo, with a total lifetime of approximately 3 h.

The environmental conditions for the bow echoes described by Schmidt and Cotton (1988), Johns and Leftwich (1988), and Smith (1990) again exhibit thermodynamic instabilities well within the range of model conditions conducive to the development of long-lived convective systems with strong surface winds (CAPEs

between 2500 and 4000 $m^2 s^{-2}$). However, these cases also exhibit between 20 and 30 m s^{-1} of vertical shear between the surface and 5 km AGL, which also clearly falls into the range of model conditions that produced long-lived bow echoes. Consistent with the model results, these convective systems remained coherent for between 6 and 12 h and, in addition, also exhibited supercell-type structures early in their lifetimes. Thus, there seems to be much similarity in the range of structures and associated environments for convective systems that produce strong surface winds over extended periods of time for both the idealized simulations and the observations.

7. Summary and discussion

We have documented herein the tendency for simulated convective systems triggered in environments of large CAPE and strong low-level vertical wind shear to evolve into bow-shaped systems of cells, similar to observational descriptions of long-lived bow echoes. For some cases, this evolution merely reflects the enhanced ability of a cold pool spreading in a vertically sheared environment to regenerate new convective cells, as described by RKW, WKR, and Weisman and Klemp (1986). In such cases, the bow shape and longevity of the convective system is directly attributed to the preferential and continual regeneration of convective cells along the downshear portion of the spreading cold air. In certain stronger-shear simulations, however, a distinct, quasi-steady structure evolves 3–4 h into the lifetime of the convective system that has yet to be described in numerical studies. This structure consists of a 40–100-km long bow-shaped system of cells with cyclonic and anticyclonic eddies (bookend vortices) at 2–3 km AGL at the northern and southern ends of the system, respectively, and a strong rear-inflow jet between the vortices. This rear-inflow jet remains elevated to near the leading edge of the convective system and plays a major role in enhancing the lifting of the potentially warm surface air ahead of the system, thus maintaining the convective circulation. The similarities between this numerically generated feature and the available observations of many severe long-lived bow echoes suggest that such systems may indeed represent a dynamically unique form of mesoconvective organization. It is this new, coherent structure that has been the focus of the current investigations.

The evolution to this new quasi-steady structure occurs systematically as the cold pool strengthens and deepens in response to the retriggering of convective cells along the leading edge of the system. As described by RKW, the cold pool–generated circulation gradually overcomes the circulation inherent in the ambient vertical wind shear, and the system begins to tilt upshear and weaken. For conditions of large CAPE and strong low-level vertical wind shear, however, the upshear tilting of the system results in the production of strong horizontal gradients of positive buoyancy aloft near the back edge of the system that generate a strong, elevated rear-inflow jet. This elevated rear inflow helps to reestablish a balance between the cold pool circulation and the ambient vertical wind shear, promoting deep forced lifting at the leading edge of the system up to jet level. Above the jet, the updraft current is then forced rearward above the spreading cold pool, thereby maintaining the buoyant plume of air aloft necessary for the maintenance of the rear-inflow structure.

The generation of this intense rear-inflow jet is also aided by the development of bookend vortices, which help to initiate and focus the rear inflow into the core of the developing system. Indeed, a long-lived bow echo–type system does not develop in these simulations without the prior existence of these features. Through an analogy with idealized two-dimensional vortex couplets, it was determined that these bookend vortices may contribute between 30% and 50% of the resultant rear-inflow strength during the system's mature phase. The primary source for this circulation is the tilting and subsequent stretching of horizontal vorticity inherent in the ambient shear layer ahead of the system, as horizontal vortex lines are deformed upward and then downward by the updraft–downdraft pattern near the ends of the convective line segment.

For the idealized bow echo, the bookend vortices originate through the splitting of the initial isolated cell and are maintained as the system expands to form a quasi-two-dimensional convective line. For the squall line example depicted in Fig. 2, however, the bookend vortices develop in situ at the ends of a preexisting convective line segment. This suggests that cell splitting, per se, is not crucial for the development of these features. In particular, bookend vortices may evolve merely as a consequence of there being physical ends to the convective system; that is, the updraft–downdraft couplet at these locations will always deform the ambient vortex lines so as to produce this flow pattern. This suggests that the development of these circulation features in squall line–type scenarios may depend somewhat randomly on whether the convective system just happens to evolve into separate convective line segments of sufficient strength to promote the further development.

The length of the resultant convective segment may also be important in this regard. As discussed in section 5b, the magnitude of the "focusing" effect for the bookend vortices decreases with increasing distance between the vortices. Thus, vortices that are spaced too far apart may not generate sufficient rear inflow to initiate the bow echo evolution. On the other hand, the smaller bow echo structure to the north in Fig. 2b was not maintained nearly as long as the larger, main bow echo feature. This suggests that an optimal length scale may exist for the development of the longest-lived bow echoes. This possibility will be investigated in future studies.

An extensive set of environmental sensitivity experiments has been completed to more clearly document the range of environmental conditions that would support bow echo genesis. These simulations suggest that convective systems similar to the idealized bow echo may be generated in environments in which the CAPE is at least 2000 $m^2 s^{-2}$ and the vertical wind shear is at least 20 m s^{-1} over the lowest 5 km AGL. In addition, the development of such systems is especially favored if most of this vertical wind shear is confined to the lowest 2.5 km AGL. The emphasis on low-level vertical wind shear occurs since such conditions produce the optimal conditions for lifting at the leading edge of the gust front. Strong vertical wind shear also supplies a significant source of horizontal vorticity to be tilted and stretched at the ends of the convective system for the production of the bookend vortices. These environmental conditions correspond closely to those that have been associated with observed severe, long-lived bow echoes and derechos.

The emphasis in the observational studies of bow echoes has been on the association between these features and the production of long-lived swaths of damaging surface winds. The current simulations reconfirm this association, but also suggest that long swaths of damaging surface winds may develop for a wider range of environmental conditions than those associated with the idealized bow echo. For the present simulations, near-surface winds of 30 m s^{-1} or greater were still being produced 4 h into the system's life for environmental CAPEs of at least 2000 $m^2 s^{-2}$ and wind variations of at least 15 m s^{-1} over the lowest 2.5–5 km AGL (20 m s^{-1} of shear was necessary for the idealized bow echoes). Since these weaker shears are more commonly observed in association with such large amounts of CAPE, many of the observed windstorm events may fall within this intermediate range of vertical wind-shear values. The convective systems in such cases, however, evolve more quickly than the stronger-shear cases, as the rear-inflow jet descends to the surface well behind the leading edge of the system, thereby promoting shallower lifting along the gust front.

The convective structures that are produced in these simulations are purely symmetrical along an axis parallel to the vertical wind-shear vector. This result is predetermined by using a unidirectional vertical wind-shear profile for the initial state and by not including the Coriolis force. As depicted in Fig. 1, however, observed bow echoes may evolve from a symmetrical structure early in their life cycle to one in which the cyclonic bookend vortex at the northern end of the system dominates over the anticyclonic bookend vortex at the southern end. This eventually produces a comma-shaped appearance to the convective rainfall pattern. Preliminary simulations suggest that the inclusion of the Coriolis force does result in the production of a dominant cyclonic vortex at the northern end of the system by 6 h, similar to the observational model. However, the basic dynamical structures described herein for first 4 h of evolution of the idealized bow echo still remain intact. These results, along with the effects of including directionally varying vertical wind shears, will also be discussed in a future study.

Another limitation to the present results is the lack of an ice phase in the model formulation. For instance, Fovell and Ogura (1988) noted that the inclusion of ice in two-dimensional squall line simulations enhanced the rearward flux of precipitation particles into the trailing portions of the storm, producing a more extensive and realistic stratiform precipitation area. Ice also tended to increase the positive potential temperature perturbations aloft due to the latent heat of fusion, thus helping to generate stronger rear-inflow circulations. These effects could have significant impacts on longer-term simulations (i.e., greater than 6 h), but have not tended to significantly impact structures produced in shorter-term simulations, as presented here.

Future studies must also consider a wider range of thermodynamic conditions than presented here, including variations to the midlevel moisture and low-level stability characteristics. The amount of midlevel moisture can affect both the strength of the convective updrafts—through the entrainment of drier, more stable air—and the strength of the convective downdrafts and rear-inflow jet—through changes to the amount of evaporation produced at the rear of the system. The net affect of these variations on a convective system, however, is difficult to gauge. As noted in the Introduction, though, severe, long-lived bow echoes are observed in environments characterized by both moist and dry midlevel conditions, suggesting that midlevel moisture content is not a critical parameter for bow echo development. Further study of the effects of low-level stability on such systems is motivated by the observation that some of these systems are generated and maintained despite very stable near-surface conditions (e.g., Schmidt and Cotton 1989).

Finally, there is strong need for observations that can confirm the structural characteristics produced in the idealized simulation. The ongoing study of Burgess and Smull (1990) supplies some of the necessary documentation, but additional case studies will be needed to verify the representativeness of these results and to extend them to more strongly sheared environments. The simulation of an observed case for which both the evolutionary and mature phases of the systems are well documented would also represent a crucial addition to this initial study. We hope, however, that the intriguing dynamical characteristics of the idealized bow echoes produced in these simulations will motivate further investigations of this type of organized mesoconvective system.

Acknowledgments. In completing this work, I have benefited greatly from conversations with and reviews of the manuscript by Richard Rotunno, Jim Fankhau-

ser, Dave Parsons, John Clark, J. Michael Fritsch, Bill Frank, Hampton N. Shirer, Bill Skamarock, and three anonymous reviewers.

APPENDIX

A Two-Dimensional Vorticity Model

In order to investigate the basic properties of vortex couplets, we have devised a simple numerical model based on a two-dimensional vorticity equation, which is derived from the inviscid, nonrotating horizontal momentum equations and the continuity equation; that is,

$$\frac{\partial u}{\partial t} + u\frac{\partial u}{\partial x} + v\frac{\partial u}{\partial y} = \frac{-1}{\rho}\frac{\partial p}{\partial x} + F_x, \quad \text{(A1)}$$

$$\frac{\partial v}{\partial t} + u\frac{\partial v}{\partial x} + v\frac{\partial v}{\partial y} = \frac{-1}{\rho}\frac{\partial p}{\partial y} + F_y, \quad \text{(A2)}$$

$$\frac{\partial u}{\partial x} + \frac{\partial v}{\partial y} = 0, \quad \text{(A3)}$$

where F_x and F_y are momentum source terms that have been included to represent some specified flow into or out of the two-dimensional plane. The vorticity equation is derived by cross differentiating (A1) and (A2), taking their difference, and using the incompressibility assumption to yield

$$\frac{\partial \zeta}{\partial t} + u\frac{\partial \zeta}{\partial x} + v\frac{\partial \zeta}{\partial y} = F(x, y), \quad \text{(A4)}$$

where ζ is defined as

$$\zeta \equiv -\frac{\partial u}{\partial y} + \frac{\partial v}{\partial x} \quad \text{(A5)}$$

and $F(x, y)$ is now an assumed distribution of vorticity forcing. Physically, $F(x, y)$ might represent the effects of localized tilting or advection of vorticity from outside the two-dimensional plane.

Since the flow is assumed to be incompressible, a streamfunction may be defined such that

$$\zeta \equiv \nabla^2\psi, \text{ where } u \equiv -\frac{\partial \psi}{\partial y} \text{ and } v \equiv \frac{\partial \psi}{\partial x}, \quad \text{(A6)}$$

and (A4) may now be rewritten as

$$\frac{\partial \zeta}{\partial t} + \frac{\partial \psi}{\partial y}\frac{\partial \zeta}{\partial x} + -\frac{\partial \psi}{\partial x}\frac{\partial \zeta}{\partial y} = F(x, y). \quad \text{(A7)}$$

This equation is solved numerically using a leapfrog time step and centered-in-space finite differences. A Dufort and Frankel time and space smoothing term is also included at each time step in order to control the growth of numerical noise (Haltiner and Williams 1980, p. 155).

The model is initialized by specifying an initial field of vorticity or vorticity forcing. At each time step, the streamfunction and thereby the velocity components are derived by solving the Poisson equation (A6) relating the streamfunction to the vorticity field. The Poisson equation is solved using a standard successive overrelaxation iteration technique (Haberman 1987, p. 516). The streamfunction and vorticity are assumed to be zero on the boundaries of the domain, yielding mirror-image symmetry across each boundary.

For the investigation of two-dimensional vortex rings, $F(x, y)$ is set to zero, and the vorticity field is initialized by specifying two circular zones of vorticity of equal magnitude but opposite sign in close proximity to each other. The strength of each vortex is defined by the following formula:

$$F = F_{\text{init}}[0.5[\cos(0.75\pi \text{RAD}_1/\text{RAD}) + 1]], \quad \text{(A8)}$$

$$\text{RAD}_1 = [(X - X_C)^2 + (Y - Y_C)^2]^{1/2}, \quad \text{(A9)}$$

where X_C and Y_C represent the coordinates of the center of each vortex. The radius of each vortex (RAD) is set at 7 km, with the magnitude of the vorticity ranging smoothly from the maximum, F_{init}, at the center of the circle to 0.15 F_{init} at the edge. Outside the circle, the vorticity is set to zero. The mean flow in the domain is set to zero, and the vortex couplet propagates as each vortex advects the other along. The domain is set at 120 km by 120 km, with a 2-km grid resolution, and the time step is set at 30 sec. Each simulation is run for 60 min. These simulations make use of the mirror-image symmetry by placing the right member of the vortex couplet preferentially near the $X = 0$ boundary. The left member is, thus, only implicitly simulated. Further information concerning these simulations and the model formulation can be found in Weisman (1990).

REFERENCES

Bluestein, H. B., and M. H. Jain, 1985: Formation of mesoscale lines of precipitation: Severe squall lines in Oklahoma during the spring. *J. Atmos. Sci.*, **42**, 1711–1732.

Burgess, D. W., and B. F. Smull, 1990: Doppler radar observations of a bow echo associated with a long-track severe windstorm. Preprints, *16th Conf. on Severe Local Storms,* Kananaskis Park, Alberta, Canada, Amer. Meteor. Soc., 203–208.

Fovell, R. G., and Y. Ogura, 1988: Numerical simulation of a mid-latitude squall line in two dimensions. *J. Atmos. Sci.*, **45**, 3846–3879.

Fujita, T. T., 1978: Manual of Downburst Identification for Project Nimrod. Satellite and Mesometeorology Research Paper No. 156, Department of Geophysical Sciences, University of Chicago, 104 pp.

Haberman, R., 1987: *Elementary Applied Partial Differential Equations with Fourier Series and Boundary Value Problems.* Prentice-Hall, 547 pp.

Haltiner, G. J., and R. T. Williams, 1980: *Numerical Prediction and Dynamic Meteorology.* Wiley & Sons, 477 pp.

Hamilton, R. E., 1970: Use of detailed intensity radar data in mesoscale surface analysis of the 4 July 1969 storm in Ohio. Preprints, *14th Conf. on Radar Meteorology,* Tucson, Amer. Meteor. Soc., 339–342.

Houze, R. A., and P. V. Hobbs, 1982: Organization and structure of precipitating cloud systems. *Advances in Geophysics,* Vol. 24, Academic Press, 225–315.

——, B. F. Smull, and P. Dodge, 1990: Mesoscale organization of springtime rainstorms in Oklahoma. *Mon. Wea. Rev.*, **118,** 613–654.

Johns, R. H., and W. D. Hirt, 1987: Derechos: widespread convectively induced windstorms. *Wea. Forecasting,* **2,** 32–49.

——, and P. W. Leftwich, Jr., 1988: The severe thunderstorm outbreak of July 28–29 1986—A case exhibiting both isolated supercells and a derecho-producing convective system. Preprints, *15th Conf. on Severe Local Storms,* Baltimore, Amer. Meteor. Soc., 448–451.

——, K. W. Howard, and R. A. Maddox, 1990: Conditions associated with long-lived derechos—An examination of the large-scale environment. Preprints, *16th Conf. on Severe Local Storms,* Kananaskis Park, Alberta, Canada, Amer. Meteor. Soc., 408–412.

Klemp, J. B., 1987: Dynamics of tornadic thunderstorms. *Ann. Rev. Fluid Mech.*, **19,** 369–402.

——, and R. B. Wilhelmson, 1978a: The simulation of three-dimensional convective storm dynamics. *J. Atmos. Sci.*, **35,** 1070–1096.

——, and ——, 1978b: Simulations of right- and left-moving storms produced through storm splitting. *J. Atmos. Sci.*, **35,** 1097–1110.

——, and D. R. Durran, 1983: An upper boundary condition permitting internal gravity wave radiation in numerical mesoscale models. *Mon. Wea. Rev.*, **111,** 430–444.

Lafore, J., and M. W. Moncrieff, 1989: A numerical investigation of the organization and interaction of the convective and stratiform regions of tropical squall lines. *J. Atmos. Sci.*, **46,** 521–544.

Maddox, R. A., 1980: Mesoscale convective complexes. *Bull. Amer. Meteor. Soc.*, **61,** 1374–1387.

Nolen, R. H., 1959: A radar pattern associated with tornadoes. *Bull. Amer. Meteor. Soc.*, **40,** 277–279.

Przybylinski, R. W., and W. J. Gery, 1983: The reliability of the bow echo as an important severe weather signature. Preprints, *13th Conf. on Severe Local Storms,* Tulsa, OK, Amer. Meteor. Soc., 270–273.

——, and D. M. DeCaire, 1985: Radar signatures associated with the derecho, a type of mesoscale convective system. Preprints, *14th Conf. Severe Local Storms,* Indianapolis, Amer. Meteor. Soc., 228–231.

Rotunno, R., and J. B. Klemp, 1982: The influence of the shear-induced pressure gradient on thunderstorm motion. *Mon. Wea. Rev.*, **110,** 136–151.

——, and ——, 1985: On the rotation and propagation of simulated supercell thunderstorms. *J. Atmos. Sci.*, **42,** 271–292.

——, ——, and M. L. Weisman, 1988: A theory for strong, long-lived squall lines. *J. Atmos. Sci.*, **45,** 463–485.

Schlesinger, R. E., 1980: A three-dimensional numerical model of an isolated deep thunderstorm. Part II: Dynamics of updraft splitting and mesovortex couplet evolution. *J. Atmos. Sci.*, **37,** 395–420.

Schmidt, J. M., and W. R. Cotton, 1989: A High Plains squall line associated with severe surface winds. *J. Atmos. Sci.*, **46,** 281–302.

Smith, B. E., 1990: Mesoscale structure of a derecho-producing convective system: The southern Great Plains storms of May 4, 1989. Preprints, *16th Conf. on Severe Local Storms,* Kananaskis Park, Amer. Meteor. Soc., 455–460.

Weisman, M. L., 1990: The genesis of bow echoes: A rear-inflow induced meso-convective structure. NCAR cooperative thesis No. 125, 148 pp. [Available from the National Center for Atmospheric Research, P.O. Box 3000, Boulder, Colorado, 80307.]

——, 1992: The role of convectively generated rear-inflow jets in the evolution of long-lived meso-convective systems. *J. Atmos. Sci.*, **49,** 1827–1847.

——, and J. B. Klemp, 1982: The dependence of numerically simulated convective storms on wind shear and buoyancy. *Mon. Wea. Rev.*, **110,** 504–520.

——, and ——, 1984: The structure and classification of numerically simulated convective storms in directionally varying wind shears. *Mon. Wea. Rev.*, **112,** 2479–2498.

——, and ——, 1986: Characteristics of isolated convective storms. *Mesoscale Meteorology and Forecasting,* Peter S. Ray, Ed., Amer. Meteor. Soc., 331–358.

——, ——, and R. Rotunno, 1988: Structure and evolution of numerically simulated squall lines. *J. Atmos. Sci.*, **45,** 1990–2013.

Wilhelmson, R. B., and C.-S. Chen, 1982: A simulation of the development of successive cells along a cold outflow boundary. *J. Atmos. Sci.*, **9,** 1466–1483.